



Tissue-resident memory CD8⁺ T cells possess unique transcriptional, epigenetic and functional adaptations to different tissue environments

John T. Crowl^{1,3}, Maximilian Heeg^{1,3}, Amir Ferry¹, J. Justin Milner¹, Kyla D. Omilusik¹, Clara Toma¹, Zhaoren He², John T. Chang^{1,2} and Ananda W. Goldrath¹✉

Tissue-resident memory T cells (T_{RM} cells) provide protective immunity, but the contributions of specific tissue environments to T_{RM} cell differentiation and homeostasis are not well understood. In the present study, the diversity of gene expression and genome accessibility by mouse CD8⁺ T_{RM} cells from distinct organs that responded to viral infection revealed both shared and tissue-specific transcriptional and epigenetic signatures. T_{RM} cells in the intestine and salivary glands expressed transforming growth factor (TGF)- β -induced genes and were maintained by ongoing TGF- β signaling, whereas those in the fat, kidney and liver were not. Constructing transcriptional-regulatory networks identified the transcriptional repressor *Hic1* as a critical regulator of T_{RM} cell differentiation in the small intestine and showed that *Hic1* overexpression enhanced T_{RM} cell differentiation and protection from infection. Provision of a framework for understanding how CD8⁺ T_{RM} cells adapt to distinct tissue environments, and identification of tissue-specific transcriptional regulators mediating these adaptations, inform strategies to boost protective memory responses at sites most vulnerable to infection.

Upon infection, naive CD8⁺ T cells become activated and subsequently undergo proliferation and differentiate to effector cells that produce inflammatory cytokines and secrete cytolytic granules. Adhesion molecules and chemokines recruit activated T cells into infected tissues. As the infection is cleared, the pathogen-specific T cell population contracts and a small number of memory T cells are retained in tissues and provide long-lived, localized immunity from reinfection (T_{RM} cells)^{1–4}. The influence of unique tissue environments on T_{RM} cell differentiation and function remains unclear.

Based on chromatin accessibility and gene expression, CD8⁺ T_{RM} precursor cells within tissues can be distinguished from both circulating effector and memory-precursor CD8⁺ T cells within the first week of infection^{5–7}. The upregulation of molecules that prevent tissue egress, CD69 and CD103, and the downregulation of lymphoid-homing molecules, including S1PR1, CCR7 and CD62L, are key for T_{RM} cell formation^{2,8}. T_{RM} cells share characteristics with circulating effector and memory CD8⁺ T cells, including expression of inflammatory cytokines and cytolytic molecules, sustained lifespan and functional protection from reinfection^{7,9}. Accordingly, T_{RM} cell differentiation requires transcription factors with well-established roles in effector (Blimp1 (ref. ¹⁰), Notch2 (ref. ¹¹) and Egr2 (ref. ¹²)) and circulating memory (Runx3 (ref. ⁵) and Nr4a1 (ref. ¹³)) CD8⁺ T cells. However, transcription factors that support differentiation of effector (T-bet) and circulating memory (Eomes) CD8⁺ T cells can suppress T_{RM} cell differentiation¹⁴. TGF- β regulates a critical nexus in these processes because it enhances tissue entry, mediates upregulation of adhesion molecules, including CD103, and contributes to downregulation of T-bet cells and Eomes^{6,14–16}.

Transcriptional networks required for tissue residency of CD8⁺ T cells are also important for the maintenance of other immune cell populations in nonlymphoid tissues, including innate lymphoid

cells (ILCs), natural killer (NK) cells and macrophages^{5,10,17,18}. Thus, T_{RM} cells may use common transcriptional modules shared among leukocytes to establish and maintain residency in nonlymphoid tissues. Elucidating a 'core' tissue-residency program has relied on identifying common features of T_{RM} cells that are distinct from circulatory T cells, but by necessity this neglects divergent gene expression arising in different nonlymphoid tissues. T cells in nonlymphoid tissues encounter varying nutrient availability, pH, oxygen tension and cytokine milieu¹⁹, and genes that vary in expression among T_{RM} cells in different tissues^{5,9,10,20,21} and mediate functional tissue adaptations have been identified. For example, skin, adipose and intestinal T_{RM} cells differentially express and depend on specific fatty acid-binding protein isoforms^{20,22}, and expression of the prototypical T_{RM} cell markers CD69 and CD103 varies across tissues. Despite these observations, tissue-specific gene-expression programs have not been comprehensively characterized for CD8⁺ T_{RM} cells.

To identify gene-expression and genome-accessibility changes that arise in CD8⁺ T cell populations responding to systemic viral infection in distinct tissues environments, we used RNA-sequencing (RNA-seq) and assay for transposase-accessible chromatin with high throughput (ATAC-seq) of cells from small intestine (SI) intraepithelial lymphocytes (IEL), kidney, liver, salivary glands (SG) and adipose tissue, as well as the spleen and blood. Single-cell (sc)RNA-seq was used to differentiate ubiquitous tissue-specific changes to the T_{RM} cell population from differences in the abundance of shared, heterogeneous T_{RM} cell populations. These results allowed prediction of tissue-specific transcriptional regulators of T_{RM} cell populations. We found that CD8⁺ T_{RM} cells from each tissue displayed unique transcriptional modules and functional activities, highlighting the critical idea that broad features of T_{RM} cells may not always be extrapolated from studies of an individual tissue and

¹Division of Biological Sciences, Department of Molecular Biology, University of California, La Jolla, CA, USA. ²Department of Medicine, University of California, La Jolla, CA, USA. ³These authors contributed equally: John T. Crowl, Maximilian Heeg. ✉e-mail: agoldrath@ucsd.edu

establishing a framework for understanding organ-specific transcriptional regulation of T_{RM} cell differentiation.

Results

T_{RM} cells show shared and tissue-specific gene-expression programs. To understand the relationship between idiosyncratic features of T_{RM} cells and the tissue environment, we infected mice with lymphocytic choriomeningitis virus (LCMV) Armstrong, which generates $CD8^+$ T_{RM} cells in a broad range of tissues¹. $CD8^+$ P14 T cells were transferred into CD45 congenic recipient mice 1 d before infection to allow for the systematic phenotyping and purification of T_{RM} cells. P14 $CD8^+$ T cells were isolated from blood, spleen, IEL, kidney, SG, liver and fat between day 30 and day 40 post-infection. Cells in the tissue were distinguished from those in the vasculature by intravenous (IV) administration of antibodies to $CD8\alpha$ before sacrifice²³. IV-negative (IV^-) P14 cells in tissues other than the spleen and blood were defined as T_{RM} cells (used as such hereafter, unless otherwise specified; Extended Data Fig. 1). We observed considerable variation in the expression of CD69 and CD103 on P14 cells isolated from tissues at days 30–40 (Fig. 1a,b). Of the tissues assessed, only IEL and SG T_{RM} cells expressed substantial levels of CD103, although the frequency of $CD103^+$ cells was considerably higher in the IEL (Fig. 1a,b). Varying frequencies of $CD69^+$ P14 cells were observed across all of the tissues, ranging from >90% in the IEL to approximately 15% in the liver (Fig. 1a,b). Similar results were observed in mice infected intravenously with *Listeria monocytogenes* that expresses the GP33 peptide (LM-GP33) (Extended Data Fig. 2a,b), indicating common differentiation and adaptation pathways associated with T_{RM} cells.

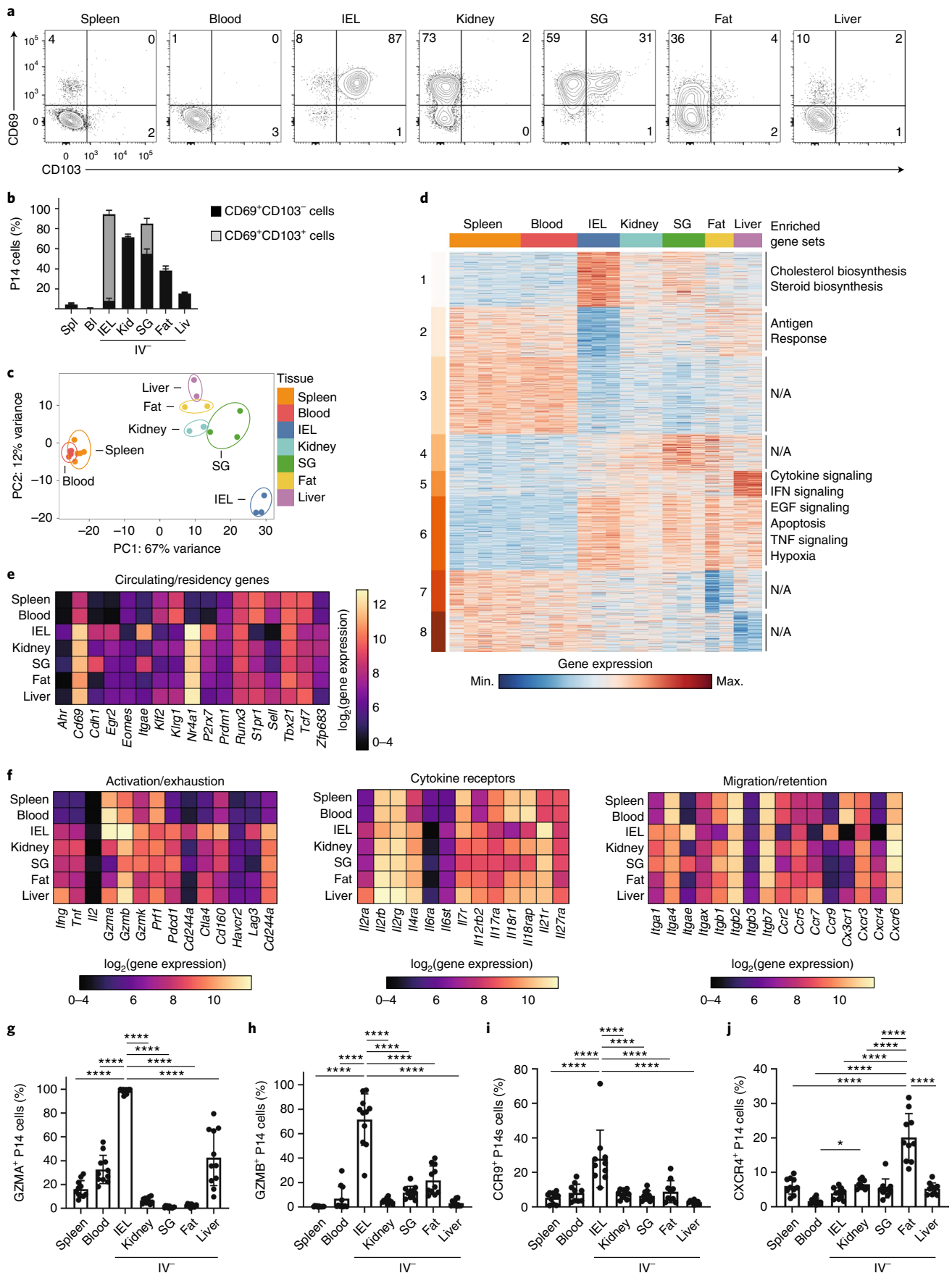
To define the transcriptional adaptations of T_{RM} cells to distinct tissue environments, we compared gene expression in P14 T cells sorted from the spleen and blood and IV^- P14 cells sorted from the IEL, kidney, liver, SG and fat at days 30–40 post-infection. Principal component analysis (PCA) of these data showed that all T_{RM} cell populations were separated distinctly from circulating P14 cells in the spleen and blood in principal component (PC)1 (Fig. 1c)^{5,6,10}. PC2 separated T_{RM} cells by tissue: liver T_{RM} cells were on one end, IEL T_{RM} cells on the opposite end and all other T_{RM} cells were distributed in between (Fig. 1c). The distance of IEL T_{RM} cells from other tissue populations indicated that they were the most transcriptionally distinct compared with the other T_{RM} cell populations. By comparing splenic P14 cells with each of the other P14 populations, we identified 2,820 differentially expressed genes (DEGs) (Fig. 1d and Supplementary Table 1). Using *k*-means clustering (*k*=8), we identified shared and tissue-specific clusters of gene expression. Clusters 3 and 6 comprised the adaptations of P14 cells to tissue residence, because these genes were differentially regulated in all T_{RM} cell populations compared with circulating P14 cells in the spleen and blood (Fig. 1d). In contrast, clusters 1, 5, 7 and 8 possessed tissue-specific, gene-expression patterns (Fig. 1d). Cluster 1 comprised genes upregulated in IEL T_{RM} cells compared with all other sequenced populations, and was enriched for genes with a role in cholesterol and steroid biosynthesis (Fig. 1d).

We next compared the expression of genes previously shown to be important for the establishment and maintenance of circulating and T_{RM} cells. T_{RM} cells in the IEL had the lowest expression of genes associated with circulating memory cells, including *Eomes*, *Tef7*, *Klf2*, *S1pr1* and *Sell*, whereas T_{RM} cells in other tissues showed intermediate expression (Fig. 1e). In addition, we compared the expression of select genes in three functional categories: genes associated with activation or exhaustion, genes encoding cytokine receptors and genes important for migration or retention (Fig. 1f). Under homeostatic conditions, we observed constitutive expression of *Gzma* in the IEL, liver, spleen and blood memory P14 $CD8^+$ T cells (Fig. 1g), with higher expression in the IEL than the liver (Fig. 1g). Granzyme B expression was high in the IEL T_{RM} cells compared with the other T_{RM} cell populations (Fig. 1h). Similar results were seen after infection with LM-GP33 (Extended Data Fig. 2c,d). IEL T_{RM} cells had high expression of *Il7r* and low expression of *Il2rb*, a component of the interleukin (IL)-2 and IL-15 receptor, compared with T_{RM} cells in the kidney, SG and fat (Fig. 1f), consistent with previous observations that kidney and SG T_{RM} cells depend on IL-15 signaling for survival, whereas IEL T_{RM} cells do not²⁴.

Within this dataset, expression of the chemokine receptors CCR9, which has a role in the recruitment of $CD8^+$ T cells to the intestine^{25,26}, and CXCR4, which mediates $CD8^+$ T cell homing to the bone marrow through interactions with CXCL12 (ref. 27), had the highest expression in T_{RM} cells isolated from the IEL and fat, respectively (Fig. 1f). We found that 25–30% of SI-resident T_{RM} cells maintained the expression of CCR9 once established in the tissue (Fig. 1i). Adipocytes can secrete CXCL12, which recruits macrophages to the tissue²⁸. T_{RM} cells isolated from adipose tissue had higher expression of CXCR4 compared with memory T cells in circulation or T_{RM} cells in other tissues (Fig. 1j), suggesting that CXCR4 may play a role in their recruitment and/or retention within adipose tissue. Analysis of published datasets^{10,20} that characterized T_{RM} cells in other experimental systems identified similar patterns of tissue-specific gene expression (Extended Data Fig. 2e,f). Compared with P14 cells in the circulation, T_{RM} cells displayed higher expression of messenger RNA for a number of genes encoding inhibitory receptors (including *Pdcd1*, *Lag3* and *Ctla4*), with IEL T_{RM} cells having the highest mRNA expression of many of these receptors (Fig. 1f). However, programmed cell death protein 1 (PD-1) or *Lag3* protein was not detected on the T_{RM} cell surface directly *ex vivo* (Extended Data Fig. 2g), suggesting that T_{RM} cells in these tissues may be poised to upregulate expression of these proteins.

Genes upregulated across T_{RM} cells in multiple tissues, such as *Fos*, *Jun* and *Nr4a1*, are upregulated by tissue digestion^{29,30}. To understand how tissue digestion impacted gene expression, we compared digestion with collagenase at 37°C with digestion with cold active protease (CAP) at 4°C. CAP digestion yielded lower numbers of T_{RM} cells than collagenase digestion and did not affect expression levels of CD69 and CD103, but cleaved $CD8\alpha$ and CD62L (Extended Data Fig. 3a,b). To determine how tissue digestion impacted the transcriptional profile, we performed RNA-seq on P14 cells isolated from the spleen and T_{RM} cells from the kidney with collagenase, CAP or dithioerythritol (DTE). We identified 620

Fig. 1 | T_{RM} cells in distinct tissue microenvironments possess unique transcriptional programs. **a,b**, Representative flow cytometry plots (**a**) and quantification (**b**) of CD69 and CD103 expression in $CD8^+$ T_{RM} cells isolated from IEL, kidney, SG, fat and liver. **c**, PCA analysis of RNA-seq of $CD8^+$ T_{RM} cells isolated from IEL, kidney, SG, fat and liver, as well as memory $CD8^+$ cells from spleen and blood. Two to three experimental replicates were used per sequenced tissue sample, generated by pooling tissues from multiple mice. **d**, Heatmap of 2,820 DEGs from RNA-seq dataset in **c**, clustered with *k*-means = 8. Enriched gene sets are indicated on the right. EGF, Epidermal growth factor; N/A, not available. **e**, The $\log_2(\text{expression})$ values for select genes previously associated with circulating or tissue-resident $CD8^+$ T cells from the RNA-seq dataset in **c**. **f**, The $\log_2(\text{expression})$ values for select genes associated with activation/exhaustion (left), cytokine receptors (center) and migration/retention (right) from the RNA-seq dataset in **c**. **g–j**, Percentage of GZMA⁺ (**g**), GZMB⁺ (**h**), CCR9⁺ (**i**) and CXCR4⁺ (**j**) P14 cells isolated from the indicated tissues as assessed by flow cytometry. Quantification of flow cytometry data in **b** and **g–j** displays the mean \pm s.d. for 12 (**b**), 11 (**g** and **h**) or 10 (**i** and **j**) mice from 3 experimental replicates. The significance was calculated using a one-way ANOVA and corrected for multiple comparisons using Tukey's test. *****P* < 0.0001.



DEGs (Extended Data Fig. 3c and Supplementary Table 2). PCA analysis showed that both digestion method and tissue defined the variation observed between samples (Extended Data Fig. 3d). Although *CD69* expression was increased in samples digested at 37°C, its expression was still elevated in CAP-digested kidney T_{RM} cells compared with splenic memory T cells (Extended Data Fig. 3e). Analysis of previously published core T_{RM} cell signatures^{5,10} indicated that some, though not all, of the genes among these signatures were additionally upregulated by digestion at 37°C (Extended Data Fig. 3f,g). Analysis of our T_{RM} cell RNA-seq dataset after removing the digestion-associated genes indicated that the T_{RM} cells in each tissue remained distinct from circulating cells, as well as each other (Extended Data Fig. 3h). Collectively, these data demonstrate that T_{RM} cells responding to the same infection possess both shared and tissue-specific, gene-expression programs and provide a basis for investigating the unique, tissue-dependent requirements for establishing this key protective population.

T_{RM} cells show inter- and intra-tissue heterogeneity. To address intra-tissue heterogeneity, we used scRNA-seq to profile circulating and T_{RM} cell populations. Spleen and blood circulating $CD8^+$ T cells were separated from T_{RM} cells on the UMAP (Uniform Manifold Approximation and Projection) dimensional reduction plot and T_{RM} cells from different tissues clustered largely separate from each other (Fig. 2a). Top genes identified as enriched in each tissue by bulk RNA-seq displayed similar patterns of gene expression in the scRNA-seq data (Extended Data Fig. 4a). In addition, the removal of digestion-associated genes from the scRNA-seq dataset did not influence the enrichment of the core T_{RM} cell signature upregulated in T cells isolated from tissues (Extended Data Fig. 5). Unbiased clustering identified 12 distinct clusters (Fig. 2b). As expected, memory $CD8^+$ T cells from spleen and blood separated into two clusters, representing cells that are more similar to effector memory T cells (T_{EM} cells) and central memory T cells (T_{CM} cells) (Fig. 2b–e). We observed analogous subsets of cells enriched for expression of effector- versus memory-associated genes among tissue-isolated T_{RM} cells to varying degrees (Fig. 2f,g and Supplementary Table 3)²¹. Cluster 3 corresponded to P14 cells in the liver that expressed memory T cell-associated genes such as *Il7r*, *Tcf7* and *Ifng*. Correspondingly, cluster 7 included liver cells that expressed effector-cell-associated genes, such as *Klrg1*, *Gzma* and *Gzmb* (Fig. 2f). Consistent with differential protein expression of CD69 and CD103 within tissues, the scRNA-seq data showed a gradient of expression for *Cd69* and *Itgae* (encoding CD103) and the tissue-resident gene signature (Extended Data Figs. 5a and 6a). In the IEL, kidney and SG, heterogeneity within a tissue correlated with additional markers of tissue residency, including the corresponding decreased expression of *Tcf7* (ref. ³¹), *Il18r1* (ref. ³²) and *Ly6c2* (ref. ³²) (Extended Data Fig. 6a,b–d). Among the most highly variable genes within each tissue, a number of genes (*Odc1*, *Rgs1* and *Dusp2*) encode for molecules with an as yet unknown function in T_{RM} cells (Extended Data Fig. 6a). Notably, in spite of the low frequency of $CD69^+$ cells among the IV^- P14 cells in the liver, the cells clustered together (Fig. 2a), arguing that the $CD69^-$ cells were not simply recirculating cells captured in the tissue. Similarly, expression of CD103 in T_{RM} cells in SG and IEL did not result in their co-clustering (Fig. 2a). Thus, the tissue origin was the most important factor in gene expression by T_{RM} cells.

Multiple genes in cluster 1 (SG), including *Pmepa1*, act as negative regulators of TGF- β signaling, whereas the upregulation of *Pmepa1* and *Xcl1* was also observed in IEL T_{RM} cells (Fig. 2f). T_{RM} cells isolated from the fat upregulated *Cxcr4* compared with T_{RM} cells isolated from other tissues (Fig. 2f,g), whereas IEL T_{RM} cells displayed elevated expression of *Itgae*, activation genes such as *Nr4a2* and *Egr1* and inhibitory receptors such as *Cd160* (Fig. 2f,g). Cluster 9 included genes upregulated during interferon (IFN) stimulation

(Fig. 2f,g). Although bulk RNA-seq indicated that P14 cells in the liver uniquely upregulated IFN- and inflammation-induced genes, scRNA-seq showed that this signature arose in only a small subset of the total cells isolated from the liver (Fig. 2f,g). Thus, scRNA-seq showed that, in spite of clear ‘on and off’ expression or heterogeneity of intracellular molecules and surface receptors, such as CD103, CD69 and IL-18 receptor (IL-18R), T_{RM} cells from a given tissue were relatively similar in overall gene expression.

Ongoing TGF- β signaling is required for SI and SG T_{RM} cells.

TGF- β is important for the formation of T_{RM} cells within diverse tissues such as the skin, SI, SG and kidney, and also plays a direct role in the upregulation of CD103 (refs. ^{6,15,16,33}). To gain insight into the range of tissues where TGF- β may shape T_{RM} cell gene expression during homeostasis, we looked for enrichment of TGF- β signaling using a published TGF- β gene-expression signature based on the in vitro treatment of $CD8^+$ T cells with TGF- β ³⁴. Cells with a high ‘TGF- β score’ were observed primarily within the IEL and SG (Fig. 3a,b), the two tissues with significant CD103 expression. To test whether sustained TGF- β signaling was important for T_{RM} cell homeostasis in a tissue-specific context, we deleted *Tgfb2* in established T_{RM} cell populations. *Tgfb2*^{fl/fl}R26-CreERT2^{-/-} or *Tgfb2*^{+/+}R26-CreERT2^{+/-} P14 (hereafter wild-type (WT)) and *Tgfb2*^{fl/fl}R26-CreERT2^{+/-} P14 cells (hereafter TGF β 2 KO) were transferred at a 1:1 ratio into congenitally distinct mice that were then infected with LCMV. Tamoxifen was administered daily from day 14 to day 18 post-infection to induce deletion of *Tgfb2* after formation of T_{RM} cells and the relative ratio WT:TGF β 2 KO cells was assessed at day 40 post-infection. We observed a twofold decrease in the relative frequency of TGF β 2 KO cells in the IEL and SG T_{RM} cell compartment compared with WT cells, with no significant loss of TGF β 2 KO $CD8^+$ P14 cells in spleen, blood, kidney, fat and liver (Fig. 3c,d). We also observed a significant decrease in the frequency of $CD103^+$ TGF β 2 KO cells compared with WT cells isolated from the IEL and SG (Fig. 3e,f). There was no decrease in the frequency of $CD69^+$ cells isolated from any of the tissues or the circulation (Fig. 3e,f). These results indicate that constitutive signaling through TGF β 2 was specifically required to maintain $CD103^+$ cells in the IEL and SG and suggests that the signals promoting T_{RM} cell survival during homeostasis were unique to each tissue.

T_{RM} cells acquire tissue-specific chromatin accessibility changes.

To gain insight into the transcription factors directing gene expression changes associated with T_{RM} cell differentiation in specific tissues, we next assessed the genome accessibility in distinct tissue environments. We performed ATAC-seq on P14 cells isolated from the spleen and IV^- P14 T_{RM} cells from the IEL, kidney, SG, fat and liver after infection with LCMV. The similarity across samples was assessed using Spearman’s correlation, and samples from the IEL and spleen clustered by replicate, whereas kidney, SG, fat and liver samples clustered among themselves (Extended Data Fig. 7a). We identified 7,150 peaks that were differentially accessible between P14 cells in the spleen and each of the other tissues (Fig. 4a, Extended Data Fig. 7b–d and Supplementary Table 4). Peaks in differentially accessible regions (DARs) were enriched within intergenic and intronic regions compared with all peaks (Extended Data Fig. 7b). We identified clusters of accessible genomic regions with tissue-specific, tissue-shared, broadly circulating and broadly resident expression profiles (Fig. 4a). To understand the relationship between DARs and DEGs, we assigned each DAR to the nearest gene, and then we assigned any differentially accessible genes to the corresponding DAR cluster. Many of these genes followed the same general pattern as the DAR with which they are associated (Fig. 4a).

Consistent with their expression patterns, the genes of canonical markers of circulation (*Sell*) and tissue residency (*Itgae* and *Ccr9*) displayed alterations in accessibility (Fig. 4b). An accessible peak

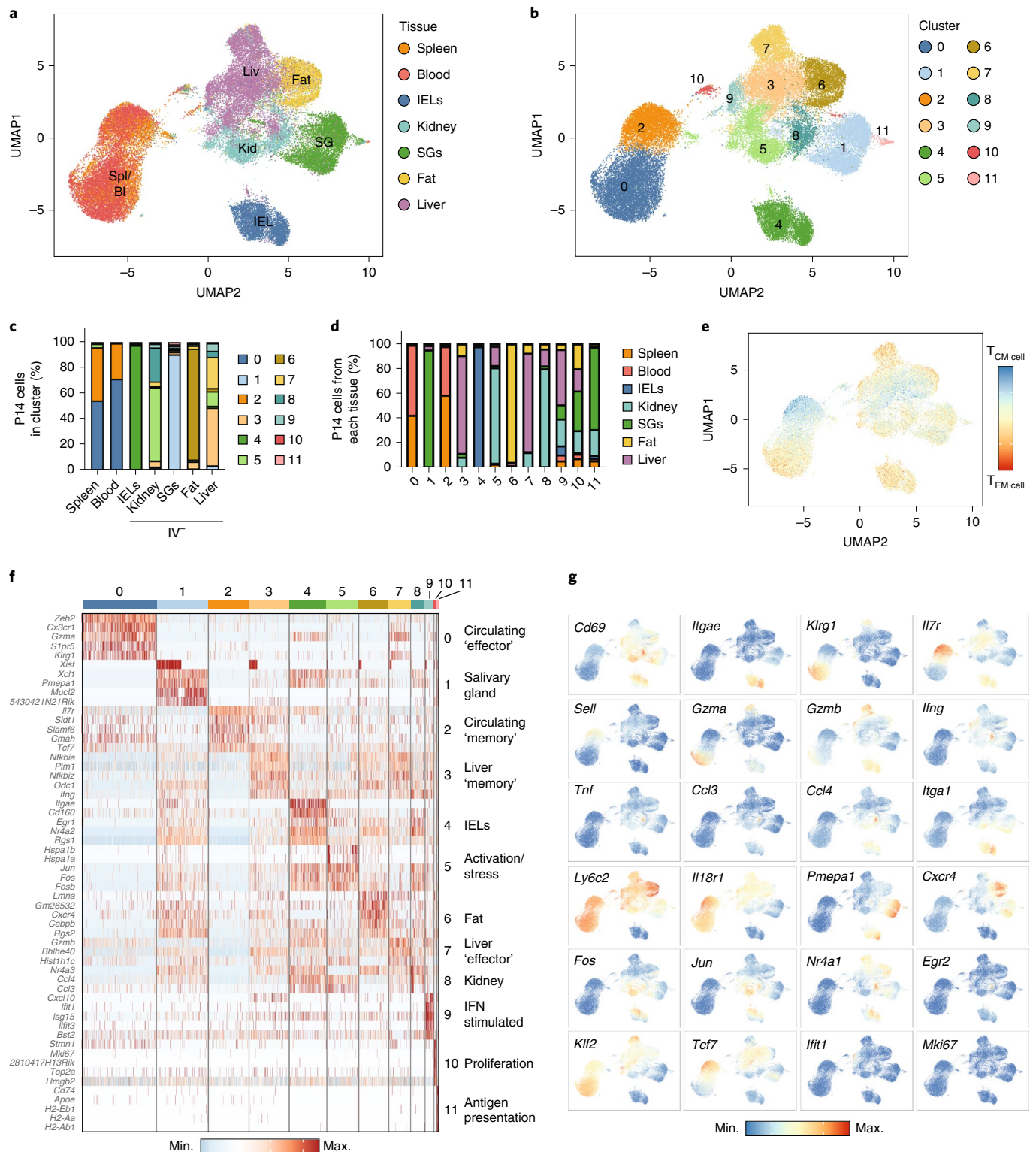


Fig. 2 | scRNA-seq identifies distinct tissue and function-specific transcriptional programs in T_{RM} cells. **a, b**, UMAP dimensional reduction colored by tissue (**a**) and cluster (**b**) of scRNA-seq of circulating and resident P14 cells isolated from the indicated tissues harvested 32 d after initial infection with LCMV. **c**, Percentage of P14 cells assigned to each cluster for each tissue for the scRNA-seq dataset in **a**. **d**, Percentage of P14 cells from each tissue in each cluster. **e**, UMAP dimensional reduction showing the difference in the T_{CM} cell or T_{EM} cell gene score for each cell. **f**, Heatmap showing the top five genes from each cluster. **g**, UMAP dimensional reduction colored by gene expression. The sequenced cells comprising each tissue in this dataset were derived from at least three experimental replicates and comprise pooled tissue samples from multiple mice.

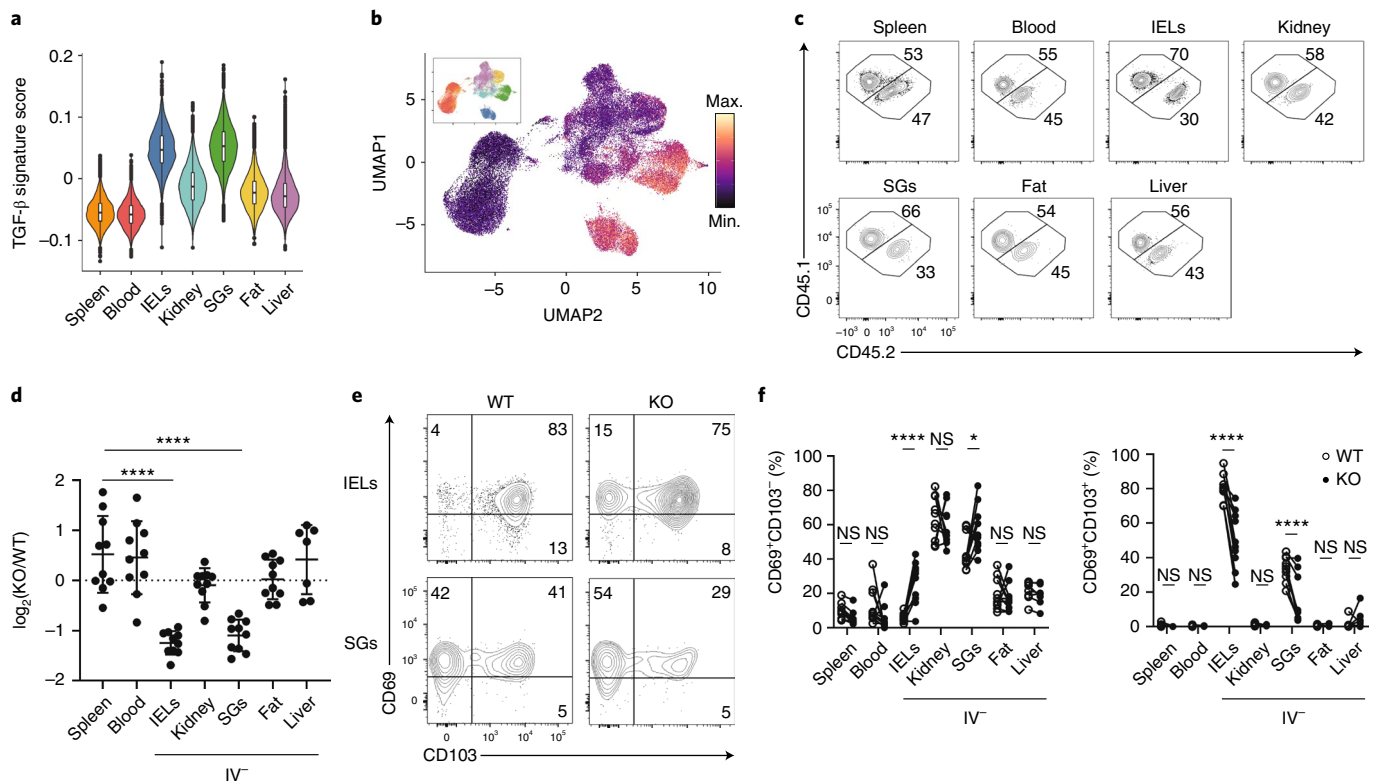


Fig. 3 | Sustained TGF- β signaling is required for the maintenance of T_{RM} cells in IEL and SG. **a, b**, Violin plot showing TGF- β signature score by tissue in scRNA-seq analysis of resident and circulating P14 cells from Fig. 2 (**a**) and UMAP dimensional reduction colored by TGF- β score (main) and tissue (inset) (**b**). **c, d**, Representative flow cytometry plots (WT CD45.1, TGF β R2 KO CD45.1.2) (**c**) and quantification (**d**) comparing relative numbers of WT and TGF β R2 KO P14 cells. **e, f**, Representative flow cytometry plots (**e**) and quantification (**f**) comparing CD69 and CD103 expression in WT and TGF β R2 KO P14 cells. Quantification of flow cytometry data in **d** and **f** displays the mean \pm s.d. for ten mice, three experimental replicates for all tissues. The boxplot in **a** shows the median. The lower and upper hinges correspond to the first and third quartiles, and the upper whisker extends from the hinge to the largest value no further than 1.5 \times interquartile range from the hinge. The significance in **d** is calculated with a one-way ANOVA and corrected for multiple comparisons using Tukey's test. The significance in **f** is calculated using a two-way ANOVA and corrected for multiple comparisons using Sidak's multiple comparison test. NS, not significant. **** $P < 0.0001$. * $P < 0.05$.

at the transcription start site (TSS) of CD62L (encoded by *Sell*) had the greatest accessibility in the P14 splenocytes. Additional accessible regions specific to both IEL and SG T_{RM} cells were identified at the TSS of *Irgae* (Fig. 4b). A uniquely accessible region in the TSS of *Ccr9* was observed in IEL T_{RM} cells (Fig. 4b), consistent with observed protein expression. In addition to the epigenetic profiling of T_{RM} cells across tissues, we assessed the expression of the transcription factors (TFs) T-bet, Eomes and Tcf1, which suppress T_{RM} cell differentiation^{14,31}. Although T-bet was downregulated in T_{RM} cells in all tissues compared with those in the circulation, Eomes was more strongly downregulated in IEL T_{RM} cells than in T_{RM} cells isolated from other sites (Fig. 4c,d). Tcf1 was downregulated in all tissue T_{RM} cells compared with circulatory memory cells, with the most prominent downregulation in the IEL, followed by the SG (Fig. 4c,d). Similarly, Tcf1 downregulation by the IEL, kidney, SG and fat T_{RM} cells compared with circulatory memory cells were observed in the response to LM-GP33 infection (Fig. 4e).

To predict key TFs that may play a role in mediating tissue-specific transcriptional programs, we used the published Taiji pipeline that had identified TFs important for the differentiation of both circulating and tissue-resident T cell populations^{5,35,36}. This approach generates a network of DARs and DEGs and predicts the TFs most likely to be driving these differences, based on the TF motif enrichment. IEL T_{RM} cells had the highest PageRank score for TFs associated with residency, including Blimp1, and a negative correlation with genes known to promote recirculation or inhibit residency, including

Klf2, Eomes and Tcf1 (Fig. 4f and Supplementary Table 5)¹⁰. In contrast, circulating memory cells in the spleen and liver T_{RM} cells were enriched for TFs associated with memory formation, including Tcf1 and Eomes (Fig. 4f). In the present study, we observed that the PageRank score indicated Runx3 activity in IEL, kidney, SG and spleen (Fig. 4f), consistent with reports on its role in both T_{RM} cell differentiation and circulating memory T cells^{5,37}. An analysis of TFs enriched across T_{RM} cells from multiple tissues compared with P14 cells from the spleen identified Nr4a1 and Jun (Fig. 4g), which have established functional roles in the formation of T_{RM} cells in vivo^{7,13}.

In the SI T_{RM} cells, PageRank identified Blimp1, which has a critical role in the formation of T_{RM} cells¹⁰. Fewer *Gzmb-Cre^{+/-}Prdm1^{fl/fl}* P14 T cells were detected in the IEL than in the kidney at day 60 post-infection with LCMV (Extended Data Fig. 8). Ahr, which is critical for maintenance of skin CD4⁺ T_{RM} and liver-resident NK cells^{38,39}, and Hic1, a ZBTB *trans*-repressor expressed in SI, but not spleen or blood leukocytes⁴⁰, were predicted to be the strongest gut-specific transcription factors by PageRank (Fig. 4g). Thus, at the epigenetic level, T_{RM} cells possessed unique and overlapping adaptations to distinct tissue environments.

Transcriptional repressor Hic1 regulates IEL T_{RM} cell formation. *Hic1* is important for the accumulation of CD4⁺ and CD8⁺ T cells in the SI under homeostatic conditions⁴⁰. We observed that *Hic1* was expressed primarily by IEL T_{RM} cells (Fig. 5a). In addition, a published scRNA-seq dataset⁷ indicated that *Hic1* was upregulated

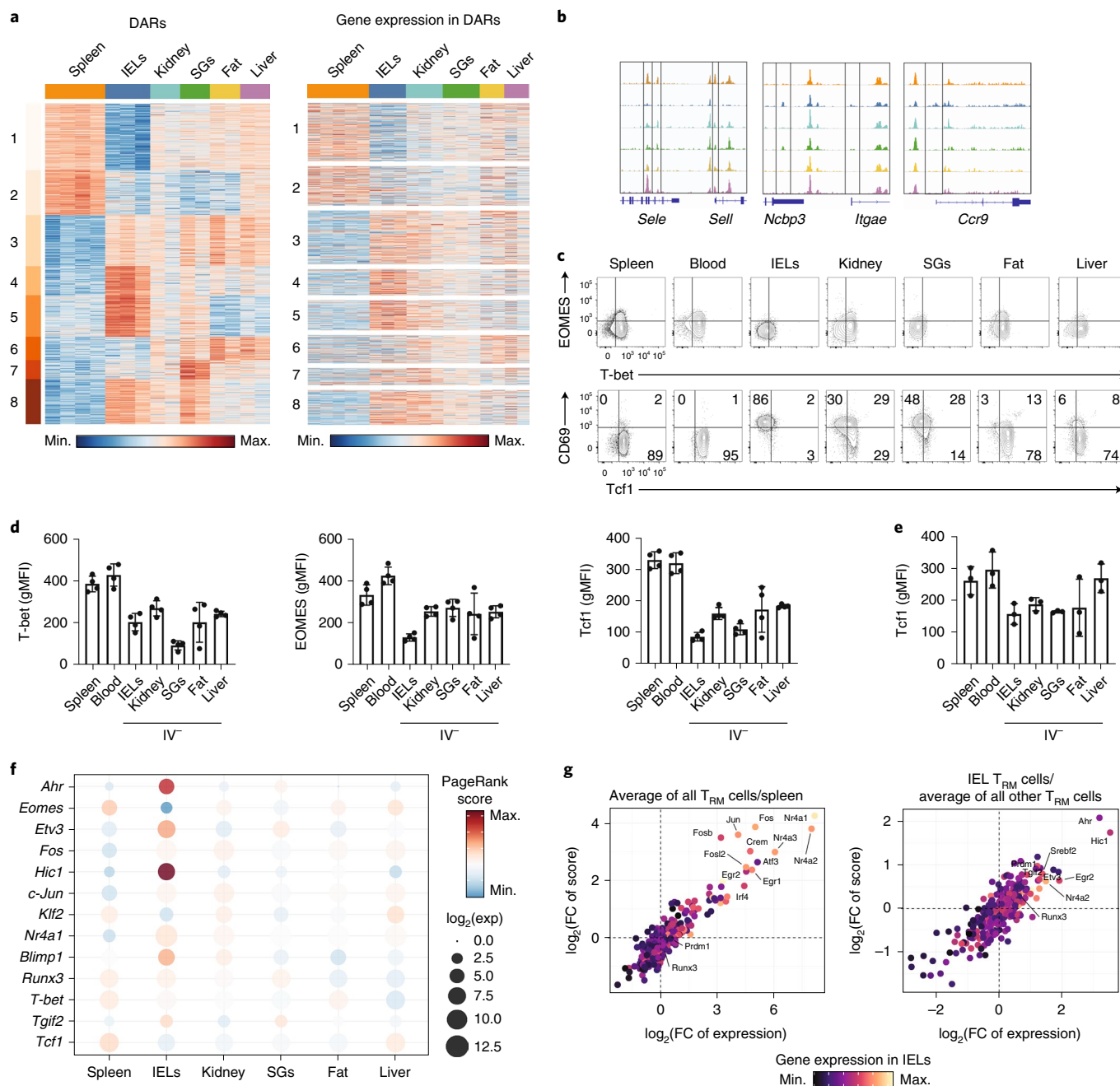


Fig. 4 | T_{RM} cells in distinct tissue microenvironments possess unique epigenetic programs. **a**, Heatmap showing 7,150 DARs clustered with k -means = 8 (left) from ATAC-seq of P14 cells in the spleen and IV⁻ P14 cells isolated from the IEL, kidney, SG, fat and liver, and gene expression for the gene nearest to each DAR (right). Only DEGs are shown. Each sequenced tissue possesses two to four experimental replicates, generated by pooling tissues from multiple mice. **b**, ATAC tracks of DARs from select genes. **c,d**, T-bet, EOMES and Tcf1 expression assessed in P14 cells isolated from mice 30–40 d after initial infection with LCMV. Flow cytometry plots (**c**) and quantification (**d**) from one representative experiment out of three total experiments with a total of eleven mice. gMFI, geometric mean of median fluorescence intensity. **e**, Tcf1 expression assessed in P14 cells isolated from mice 30–34 d after initial infection with LM-GP33. Quantification is from one representative experiment out of three experiments with a total of ten mice. **f**, PageRank score and gene expression for select TFs displayed by individual tissues. **g**, Average PageRank score and gene expression of transcription factors displayed as the average in all T_{RM} cells over P14 cells in the spleen (left) PageRank score and gene expression in IEL T_{RM} cells over the average of all other T_{RM} cells (right). FC, fold-change.

at early timepoints (day 5) post-infection with LCMV and maintained until at least 90 d post-infection in SI CD8⁺ T_{RM} cells (Fig. 5b). Further analysis of published datasets indicated that *Hic1* was upregulated in SI-resident CD4⁺ T cells⁴¹, macrophages¹⁷ and type 2 innate lymphocytes (ILC2s)⁴² compared with these cell types in other tissues (Extended Data Fig. 9a), suggesting common adaptation by diverse cell types to SI residency.

To determine whether *Hic1* had a specific role in the formation of SI T_{RM} cells, activated P14 CD8⁺ T cells transduced with a retroviral vector encoding CD19–short hairpin (sh)RNA as control (Ctrl) or *Hic1*–shRNA (*Hic1* KD) were mixed at a 1:1 ratio and adoptively transferred into recipient mice 1 h before infection with LCMV. At days 7–8 post-infection, the percentage of *Hic1* KD cells was increased relative to Ctrl cells in the SG, whereas their

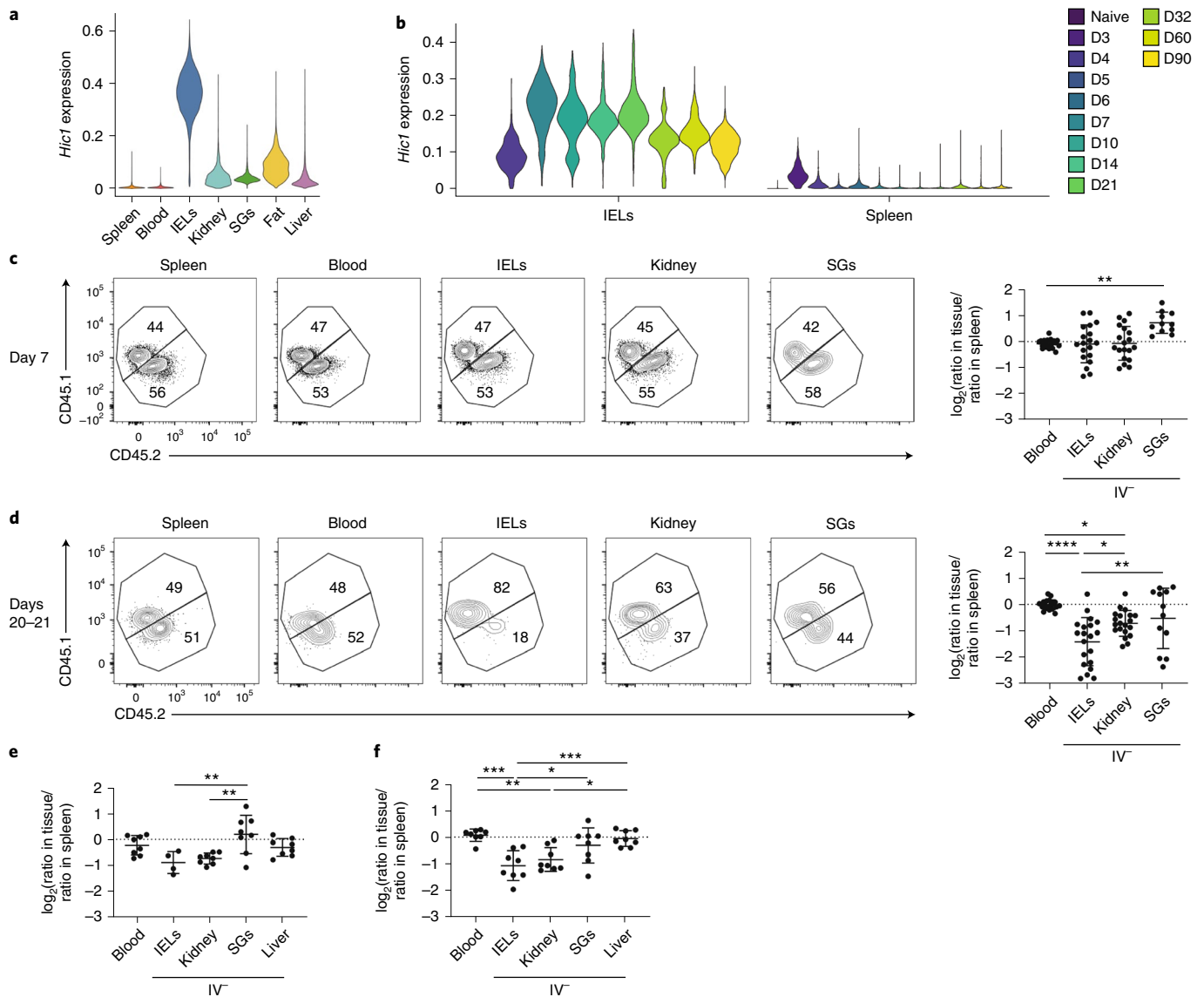


Fig. 5 | Loss of *Hic1* prevents the formation of SI T_{RM} cells. **a**, Violin plots displaying *Hic1* expression after MAGIC imputation in scRNA-seq data from Fig. 2. **b**, *Hic1* expression in scRNA-seq dataset from Kurd et al.⁷. The violin plot is colored by time after infection with LCMV. D, Day. **c-f**, A 1:1 mixed transfer of P14 cells transduced with a control shRNA or a *Hic1*-targeting shRNA before infection with LCMV or LM-GP33. Representative flow cytometry plot (Ctrl CD45.1, *Hic1* KD CD45.1.2) (left) and quantification (right) of the relative ratios between *Hic1*-targeting and control shRNAs are normalized to the spleen on days 7–8 (**c**) or 20–21 (**d**) after initial infection with LCMV. **e, f**, Quantification of the relative ratios between *Hic1*-targeting and control shRNAs normalized to the spleen on day 7 (**e**) or day 20 (**f**) after initial infection with LM-GP33. Graphs in **c** and **d** display the mean \pm s.d. for 19 mice from 5 separate experiments for blood, spleen, IEL and kidney, and 11 mice from 3 experiments for SG. Graphs in **e** and **f** display the mean \pm s.d. for eight mice from two separate experiments. The significance was calculated using a one-way ANOVA and corrected for multiple comparisons using Tukey’s test. * $P < 0.05$, ** $P < 0.01$, *** $P < 0.001$, **** $P < 0.0001$.

frequencies were similar in all the other tissues (Fig. 5c). At days 20–21 post-infection we observed a decrease in the fraction of *Hic1* KD cells in the kidney and an even greater decrease in the SI compared with Ctrl cells (Fig. 5d). Similarly, the frequency of *Hic1* KD cells was increased in the SG compared with Ctrl cells at day 7 post-infection with LM-GP33 (Fig. 5e), whereas *Hic1* KD cells were reduced in the IEL and kidney at day 20 (Fig. 5e,f). The percentage of CD69⁺CD103⁻ and CD69⁺CD103⁺ *Hic1* KD and Ctrl cells were similar at days 7–8 and days 20–21 post-LCMV infection in the IEL and kidney (Extended Data Fig. 9b,c), whereas the percentage of CD69⁺CD103⁻ cells in the kidney and the percentage of CD69⁺CD103⁺ cells in the IEL were reduced among *Hic1* KD compared with Ctrl cells at day 20 post-infection with

LM-GP33 (Extended Data Fig. 9d). There was no change in the relative fraction of *Hic1* KD KLRG1⁺CD127⁻ terminal effector (TE), KLRG1⁻CD127⁺ memory precursor (MP), CD127⁻CD62L⁻ t- T_{EM} , CD127⁺CD62L⁻ T_{EM} and CD127⁺CD62L⁺ T_{CM} cells post-LCMV infection at day 7 and days 20–21, whereas there was a small, but significant, decrease in *Hic1* KD T_{EM} cells and a significant small increase in *Hic1* KD T_{CM} cells compared with Ctrl cells at day 20 post-LM-GP33 infection (Extended Data Fig. 9e–h), suggesting that memory T cell formation in the absence of *Hic1* might be influenced by the kinetics or type of infection.

Next, P14 cells transduced with either an empty retroviral vector (Ctrl) or a retroviral vector encoding *Hic1* cDNA (*Hic1* OE) were mixed at a 1:1 ratio and adoptively transferred into recipient

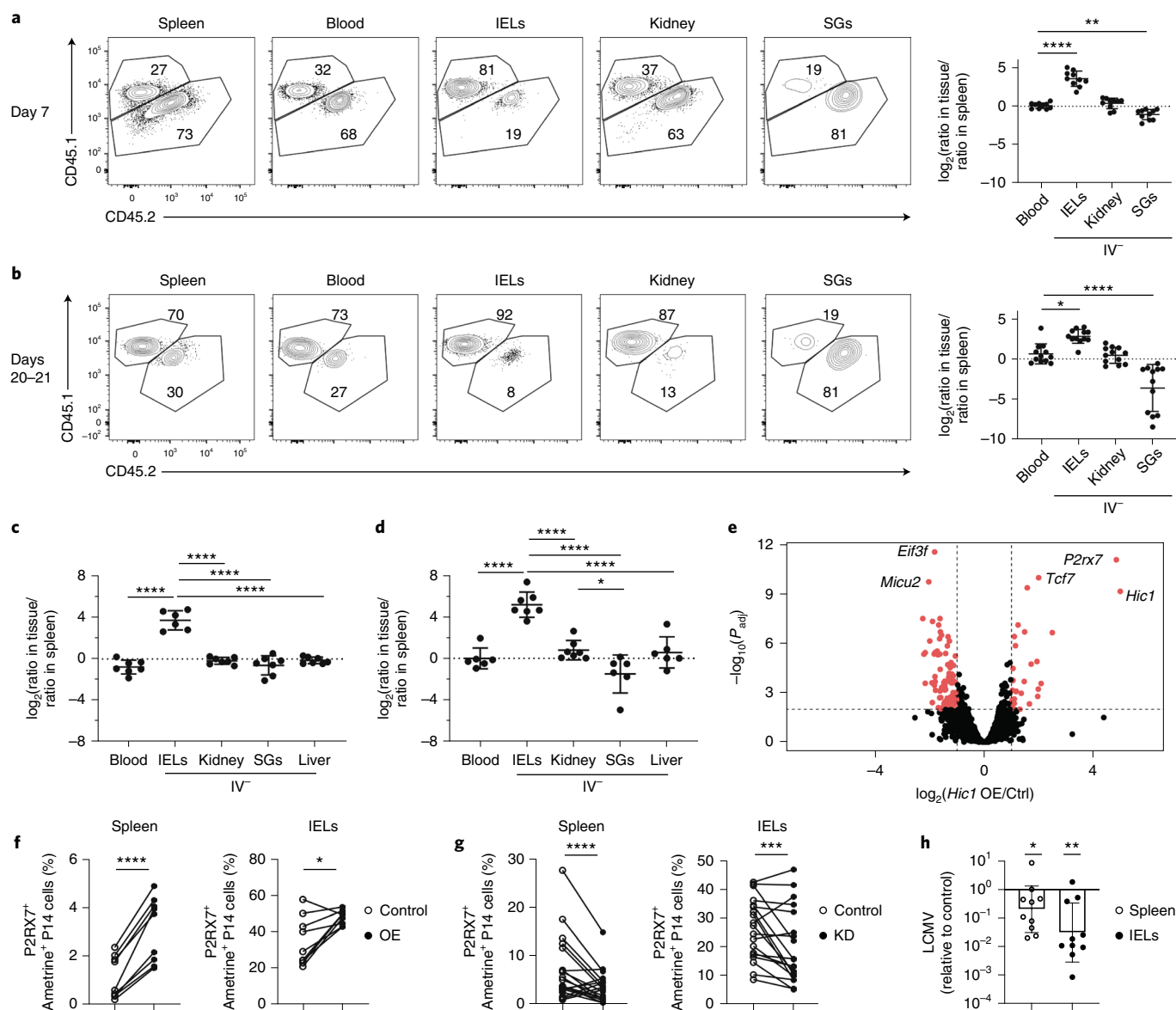


Fig. 6 | *Hic1* overexpression enhances the formation of SI TRM cells. a–d, A 1:1 mixed transfer of P14 cells transduced with a control or a *Hic1*-overexpression construct before infection with LCMV or LM-GP33. Representative flow cytometry plot (Ctrl CD45.1.2, *Hic1* KD CD45.1) (left) and quantification (right) of the relative ratios between *Hic1* and control-transduced P14 cells are normalized to the spleen on days 7–8 (**a**) or days 20–21 (**b**) after initial infection with LCMV. Quantification of the relative ratios between *Hic1* and control-transduced P14 cells was normalized to the spleen on day 7 (**c**) or day 20 (**d**) after initial infection with LM-GP33. **e**, RNA-seq of control and *Hic1*-overexpressing P14 cells isolated from the spleen at day 7 post-infection with LCMV. **f, g**, Percentage of P2RX7⁺ ametrine⁺ P14 cells isolated from the spleen (left) or IEL (right) in *Hic1*-overexpression at day 7 post-infection (**f**) and in *Hic1* knockdown at day 7 post-infection (**g**). **h**, Bar plot showing LCMV expression in mice that received *Hic1*-overexpressing P14 cells normalized to mice receiving control P14 cells. LCMV titers were assessed by qPCR relative to HPRT. Graphs in **a** and **b** display the mean \pm s.d. from 10 mice (**a**) and 12 mice (**b**) from 3 separate experiments. Graphs in **c** and **d** display the mean \pm s.d. for six mice (**c**) and seven mice (**d**) from two separate experiments. Significance in **a–d** was calculated using a one-way ANOVA and corrected for multiple comparisons using Tukey's test. Graphs in **f** display three individual experiments with three mice each. Graphs in **g** display mean \pm s.d. for 18 mice from 4 separate experiments. Significance in **f** and **g** was calculated using a two-sided, paired Student's *t*-test and connecting lines indicate that the Ctrl and *Hic1* KD/OE cells were isolated from the same mouse. The graph in **h** displays the geometric mean \pm s.d. from two different experiments with five mice each. The significance was calculated using an unpaired, two-sided Student's *t*-test. **P* < 0.05, ***P* < 0.01, ****P* < 0.001, *****P* < 0.0001.

mice 1 h before infection with LCMV. At day 7 post-infection, the frequency of *Hic1* OE cells in the IEL was approximately 11-fold higher than in *Hic1* OE cells in the spleen (Fig. 6a,b). At day 20 post-infection, the frequency of *Hic1* OE cells was higher compared with Ctrl cells in the spleen, blood, kidney and IEL, whereas *Hic1* OE cells were greatly reduced in the SG (Fig. 6b). A similar increase in the percentage of *Hic1* OE IEL cells and a decrease in the percentage

of *Hic1* OE SG cells compared with Ctrl cells were observed at days 7 and 20 post-infection with LM-GP33 (Fig. 6c,d). We detected a greater frequency of CD69⁺CD103⁺ *Hic1* OE cells compared with Ctrl cells in the IEL at day 7, but not day 21 post-LCMV infection (Extended Data Fig. 9i,j). We also detected increased frequency of *Hic1* OE MP cells and decreased frequency of *Hic1* OE TE cells at day 7 post-infection (Extended Data Fig. 9k)⁴³, and increased

frequency of *Hic1* OE T_{EM} cells and decreased frequency of *Hic1* OE T_{CM} cells at day 21 (Extended Data Fig. 9l).

To assess how *Hic1* mediated these effects, we performed RNA-seq on *Hic1* OE cells and Ctrl cells sorted from the spleen at day 7 post-LCMV infection. We observed elevated expression of *P2rx7*, an ATP receptor important for memory T cell differentiation and T_{RM} cell homeostasis^{43,44}, in *Hic1* OE cells (Fig. 6e and Supplementary Table 6). A higher percentage of *Hic1* OE cells in the spleen and IEL was P2RX7⁺ compared with Ctrl cells in the same tissues (Fig. 6f), whereas both splenic and IEL *Hic1* KD cells had decreased expression of P2RX7 (Fig. 6g). Expression of *P2rx7* was highest in SI CD8⁺ T_{RM} cells, CD4⁺ T_{RM} cells, macrophages and ILC2s compared with the corresponding resident populations in other sites (Extended Data Fig. 9m).

To assess the functional capacity of P14 cells that overexpressed *Hic1*, Ctrl cells or *Hic1* OE cells were adoptively transferred into distinct recipients 1 h before intravenous infection with LM-GP33, followed by LCMV infection on day 20 post-LM-GP33 infection. The quantitative (q)PCR assessment of viral load at day 3 post-LCMV infection indicated a reduction in LCMV titers in the spleen, and even more in the SI, in mice that received *Hic1* OE cells compared with those receiving Ctrl cells (Fig. 6h). Of note, analysis of gene expression in a human scRNA-seq dataset showed enrichment of the core T_{RM} cells and TGF- β -induced gene-expression signatures⁴⁵, as well as elevated *Hic1* expression in T cells isolated from the intestine and rectum compared with peripheral blood mononuclear cells (Extended Data Fig. 10). These observations indicated that *Hic1* was critical for establishing a mature T cell population in the SI, and that its expression could be detrimental to the formation of T_{RM} cells in other tissues. Thus, parallel transcriptional pathways may support both mouse and human T_{RM} cell populations and favor seeding as well as maintenance of resident T cell populations in a particular tissue.

Discussion

In the present study, we showed that T_{RM} cells in distinct tissues possessed transcriptional and epigenetic programs that comprised both broadly shared tissue-resident and tissue-specific signatures. We observed variances in T_{RM} cell populations that included the differential expression of and dependence on genes known to be important for the generation and function of T_{RM} cells, and we identified previously unknown tissue-specific transcriptional regulators. Our observations highlighted the broad functional, transcriptional and epigenetic adaptations of T_{RM} cells with the same antigen specificity to a range of tissue environments, thus establishing a framework for identifying targets that influence T_{RM} cell populations within specific organs to enhance therapeutic strategies.

Using RNA-seq, scRNA-seq and ATAC-seq assays, we observed that T_{RM} cells from each tissue were more similar to each other than to circulating memory T cells of the same pathogen specificity, with T_{RM} cells from the IEL being most distinct. ScRNA-seq revealed substantial heterogeneity in the expression of numerous genes among T_{RM} cells within a tissue, consistent with previous reports of intra-tissue functional heterogeneity^{7,9,46}. Ultimately, the systematic comparison of gene expression and chromatin accessibility across T_{RM} cell populations emphasized the idea that statements about the generation, function and homeostasis of T_{RM} cell populations need to consider the tissue-specific context in each case.

TGF- β is a pleiotropic cytokine known to affect transcriptional programs at barrier sites and is important for the formation of T_{RM} cells in diverse tissues, including the skin, SI, kidney and SG^{6,8,14–16,34}. The TGF- β -induced gene expression signature in IEL and SG T_{RM} cells persisted long after T_{RM} cell formation and viral clearance, indicating that ongoing TGF- β signaling is important for T_{RM} cell maintenance in a tissue-specific manner. We found that the loss of TGF β R2 resulted in decreased numbers of T_{RM} cells in the IEL and

SG, but not the kidney or liver, consistent with reports that ongoing TGF- β signaling is also required for maintenance of T_{RM} cells within the epidermis but not the liver¹⁷. These findings further highlight the previously underestimated differences across T_{RM} cell populations from their residing tissues.

Leveraging gene expression and chromatin accessibility data, the PageRank algorithm identified known T_{RM} cell regulators, such as Ahr, Blimp1 and Nr4a1, and the transcriptional repressor *Hic1* as one of the top predicted regulators of differential gene expression in SI T_{RM} cells. We found that *Hic1* expression regulated T_{RM} cell formation, particularly in the SI. Loss of *Hic1* did not prevent T cell access to the SI, but resulted in defective T_{RM} cell persistence in the SI and a partial loss of kidney T_{RM} cells, whereas overexpression of *Hic1* led to increased accumulation of T_{RM} cells in the SI. *Hic1* overexpression led to a significant decrease in established T_{RM} cells in the SG, indicating that adaptation to one tissue may impair T_{RM} cell homeostasis in another environment. *Hic1* mediated changes in expression of P2RX7, a sensor of damage-associated molecular patterns shown to play an important role in T_{RM} cell formation^{43,44,48}. *Hic1*-overexpressing CD8⁺ T_{RM} cells had higher expression of P2RX7 than controls and *Hic1* knockdown resulted in lower expression of P2RX7, suggesting that *Hic1* may regulate adaptation to the SI environment. Both *Hic1* and P2RX7 are induced by retinoic acid, which is produced by the intestinal epithelium and promotes the differentiation of gut-homing immune cells and collaborates with TGF- β in promoting mucosal immunity^{40,49–51}. Thus, the tissue milieu may provide additional remodeling of transcriptional networks that promote adaptation to that specific tissue.

In addition to the CD8⁺ T_{RM} cells, immune cells such as ILCs, macrophages, NK cells and CD4⁺ T cells have permanent residence in many tissues^{3,10,17,18}. Blimp1 and Hobit collaborate to promote tissue residency of CD8⁺ T_{RM}, NK and NKT cells by repressing genes associated with circulation and tissue egress¹⁰. Comparing expression of *Hic1* across CD8⁺ T cells, CD4⁺ T cells, ILC2s, NK cells and macrophages indicated the tissue-specific upregulation of *Hic1* by cells in the SI compared with immune cells in other tissues, supporting the idea of a broad role for *Hic1* in establishing the resident immune program in the SI^{17,41,42,52}. Similarly, organ-specific expression of fatty acid-binding protein isoforms in CD8⁺ T_{RM} cells is driven by secreted factors derived from the tissues and this expression is mirrored by other resident immune cell types within each organ¹⁷. Thus, in addition to providing an atlas of distinct and overlapping T_{RM} cell features in diverse tissue environments, these findings collectively raise the possibility of ‘programming’ tissue-tailored immune responses, where immune cells that promote or regulate inflammation could be transcriptionally engineered for trafficking to, retention in and function within a particular tissue.

Online content

Any methods, additional references, Nature Research reporting summaries, extended data, supplementary information, acknowledgements, peer review information; details of author contributions and competing interests; and statements of data and code availability are available at <https://doi.org/10.1038/s41590-022-01229-8>.

Received: 4 August 2021; Accepted: 26 April 2022;

Published online: 27 June 2022

References

- Steinert, E. M. et al. Quantifying memory CD8 T cells reveals regionalization of immunosurveillance. *Cell* **161**, 737–749 (2015).
- Skon, C. N. et al. Transcriptional downregulation of *S1pr1* is required for the establishment of resident memory CD8⁺ T cells. *Nat. Immunol.* **14**, 1285–1293 (2013).
- Gebhardt, T. et al. Memory T cells in nonlymphoid tissue that provide enhanced local immunity during infection with herpes simplex virus. *Nat. Immunol.* **10**, 524–530 (2009).

4. Masopust, D. & Soerens, A. G. Tissue-resident T cells and other resident leukocytes. *Annu. Rev. Immunol.* **37**, 521–546 (2019).
5. Milner, J. J. et al. Runx3 programs CD8⁺ T cell residency in non-lymphoid tissues and tumours. *Nature* **552**, 253–257 (2017).
6. Mackay, L. K. et al. The developmental pathway for CD103⁺CD8⁺ tissue-resident memory T cells of skin. *Nat. Immunol.* **14**, 1294–1301 (2013).
7. Kurd, N. S. et al. Early precursors and molecular determinants of tissue-resident memory CD8⁺ T lymphocytes revealed by single-cell RNA sequencing. *Sci. Immunol.* **5**, eaaz6894 (2020).
8. Casey, K. A. et al. Antigen-independent differentiation and maintenance of effector-like resident memory T cells in tissues. *J. Immunol.* **188**, 4866–4875 (2012).
9. Milner, J. J. et al. Heterogenous populations of tissue-resident CD8⁺ T cells are generated in response to infection and malignancy. *Immunity* **52**, 808–824.e807 (2020).
10. Mackay, L. K. et al. Hobit and Blimp1 instruct a universal transcriptional program of tissue residency in lymphocytes. *Science* **352**, 459–463 (2016).
11. Hombink, P. et al. Programs for the persistence, vigilance and control of human CD8⁺ lung-resident memory T cells. *Nat. Immunol.* **17**, 1467–1478 (2016).
12. Du, N. et al. EGR2 is critical for peripheral naive T-cell differentiation and the T-cell response to influenza. *Proc. Natl Acad. Sci. USA* **111**, 16484–16489 (2014).
13. Boddupalli, C. S. et al. ABC transporters and NR4A1 identify a quiescent subset of tissue-resident memory T cells. *J. Clin. Invest.* **126**, 3905–3916 (2016).
14. Mackay, L. K. et al. T-box transcription factors combine with the cytokines TGF-beta and IL-15 to control tissue-resident memory T cell fate. *Immunity* **43**, 1101–1111 (2015).
15. Ma, C., Mishra, S., Demel, E. L., Liu, Y. & Zhang, N. TGF-beta controls the formation of kidney-resident T cells via promoting effector T cell extravasation. *J. Immunol.* **198**, 749–756 (2017).
16. Zhang, N. & Bevan, M. J. Transforming growth factor-beta signaling controls the formation and maintenance of gut-resident memory T cells by regulating migration and retention. *Immunity* **39**, 687–696 (2013).
17. Lavin, Y. et al. Tissue-resident macrophage enhancer landscapes are shaped by the local microenvironment. *Cell* **159**, 1312–1326 (2014).
18. Frizzell, H. et al. Organ-specific isoform selection of fatty acid-binding proteins in tissue-resident lymphocytes. *Sci. Immunol.* **5**, eaay9283 (2020).
19. Krausgruber, T. et al. Structural cells are key regulators of organ-specific immune responses. *Nature* **583**, 296–302 (2020).
20. Han, S. J. et al. White adipose tissue is a reservoir for memory T cells and promotes protective memory responses to infection. *Immunity* **47**, 1154–1168.e1156 (2017).
21. Milner, J. J. et al. Delineation of a molecularly distinct terminally differentiated memory CD8 T cell population. *Proc. Natl Acad. Sci. USA* **117**, 25667–25678 (2020).
22. Pan, Y. et al. Survival of tissue-resident memory T cells requires exogenous lipid uptake and metabolism. *Nature* **543**, 252–256 (2017).
23. Anderson, K. G. et al. Intravascular staining for discrimination of vascular and tissue leukocytes. *Nat. Protoc.* **9**, 209–222 (2014).
24. Schenkel, J. M. et al. IL-15-Independent maintenance of tissue-resident and boosted effector memory CD8 T cells. *J. Immunol.* **196**, 3920–3926 (2016).
25. Svensson, M. et al. CCL25 mediates the localization of recently activated CD8alpha⁺ lymphocytes to the small-intestinal mucosa. *J. Clin. Invest.* **110**, 1113–1121 (2002).
26. Zabel, B. A. et al. Human G protein-coupled receptor GPR-9-6/CC chemokine receptor 9 is selectively expressed on intestinal homing T lymphocytes, mucosal lymphocytes, and thymocytes and is required for thymus-expressed chemokine-mediated chemotaxis. *J. Exp. Med.* **190**, 1241–1256 (1999).
27. Mazo, I. B. et al. Bone marrow is a major reservoir and site of recruitment for central memory CD8⁺ T cells. *Immunity* **22**, 259–270 (2005).
28. Kim, D. et al. CXCL12 secreted from adipose tissue recruits macrophages and induces insulin resistance in mice. *Diabetologia* **57**, 1456–1465 (2014).
29. Adam, M., Potter, A. S. & Potter, S. S. Psychrophilic proteases dramatically reduce single-cell RNA-seq artifacts: a molecular atlas of kidney development. *Development* **144**, 3625–3632 (2017).
30. O’Flanagan, C. H. et al. Dissociation of solid tumor tissues with cold active protease for single-cell RNA-seq minimizes conserved collagenase-associated stress responses. *Genome Biol.* **20**, 210 (2019).
31. Wu, J. et al. T cell factor 1 suppresses CD103⁺ lung tissue-resident memory T cell development. *Cell Rep.* **31**, 107484 (2020).
32. Liao, W. et al. The downregulation of IL-18R defines bona fide kidney-resident CD8⁺ T cells. *iScience* **24**, 101975 (2021).
33. Thom, J. T., Weber, T. C., Walton, S. M., Torti, N. & Oxenius, A. The salivary gland acts as a sink for tissue-resident memory CD8⁺ T cells, facilitating protection from local cytomegalovirus infection. *Cell Rep.* **13**, 1125–1136 (2015).
34. Nath, A. P. et al. Comparative analysis reveals a role for TGF-beta in shaping the residency-related transcriptional signature in tissue-resident memory CD8⁺ T cells. *PLoS ONE* **14**, e0210495 (2019).
35. Yu, B. et al. Epigenetic landscapes reveal transcription factors that regulate CD8⁺ T cell differentiation. *Nat. Immunol.* **18**, 573–582 (2017).
36. Zhang, K., Wang, M., Zhao, Y. & Wang, W. Taiji: system-level identification of key transcription factors reveals transcriptional waves in mouse embryonic development. *Sci. Adv.* **5**, eaav3262 (2019).
37. Wang, D. et al. The transcription factor Runx3 establishes chromatin accessibility of cis-regulatory landscapes that drive memory cytotoxic T lymphocyte formation. *Immunity* **48**, 659–674.e656 (2018).
38. Zaid, A. et al. Persistence of skin-resident memory T cells within an epidermal niche. *Proc. Natl Acad. Sci. USA* **111**, 5307–5312 (2014).
39. Khan, T. N., Mooster, J. L., Kilgore, A. M., Osborn, J. F. & Nolz, J. C. Local antigen in nonlymphoid tissue promotes resident memory CD8⁺ T cell formation during viral infection. *J. Exp. Med.* **213**, 951–966 (2016).
40. Burrows, K. et al. The transcriptional repressor HIC1 regulates intestinal immune homeostasis. *Mucosal Immunol.* **10**, 1518–1528 (2017).
41. Beura, L. K. et al. CD4⁺ resident memory T cells dominate immunosurveillance and orchestrate local recall responses. *J. Exp. Med.* **216**, 1214–1229 (2019).
42. Ricardo-Gonzalez, R. R. et al. Tissue signals imprint ILC2 identity with anticipatory function. *Nat. Immunol.* **19**, 1093–1099 (2018).
43. Borges da Silva, H. et al. The purinergic receptor P2RX7 directs metabolic fitness of long-lived memory CD8⁺ T cells. *Nature* **559**, 264–268 (2018).
44. Borges da Silva, H. et al. Sensing of ATP via the purinergic receptor P2RX7 promotes CD8⁺ T_{RM} cell generation by enhancing their sensitivity to the cytokine TGF-beta. *Immunity* **53**, 158–171.e156 (2020).
45. Boland, B. S. et al. Heterogeneity and clonal relationships of adaptive immune cells in ulcerative colitis revealed by single-cell analyses. *Sci. Immunol.* **5**, eabb4432 (2020).
46. Milner, J. J. & Goldrath, A. W. Transcriptional programming of tissue-resident memory CD8⁺ T cells. *Curr. Opin. Immunol.* **51**, 162–169 (2018).
47. Mani, V. et al. Migratory DCs activate TGF-beta to precondition naive CD8⁺ T cells for tissue-resident memory fate. *Science* **366**, eaav5728 (2019).
48. Stark, R. et al. T_{RM} maintenance is regulated by tissue damage via P2RX7. *Sci. Immunol.* **3**, eaau1022 (2018).
49. Hashimoto-Hill, S., Friesen, L., Kim, M. & Kim, C. H. Contraction of intestinal effector T cells by retinoic acid-induced purinergic receptor P2X7. *Mucosal Immunol.* **10**, 912–923 (2017).
50. Mucida, D., Park, Y. & Cheroutre, H. From the diet to the nucleus: vitamin A and TGF-beta join efforts at the mucosal interface of the intestine. *Semin. Immunol.* **21**, 14–21 (2009).
51. Heiss, K. et al. High sensitivity of intestinal CD8⁺ T cells to nucleotides indicates P2X7 as a regulator for intestinal T cell responses. *J. Immunol.* **181**, 3861–3869 (2008).
52. McFarland, A. P. et al. Multi-tissue single-cell analysis deconstructs the complex programs of mouse natural killer and type 1 innate lymphoid cells in tissues and circulation. *Immunity* **54**, 1320–1337.e1324 (2021).

Publisher’s note Springer Nature remains neutral with regard to jurisdictional claims in published maps and institutional affiliations.

© Springer Nature America, Inc. 2022

Methods

Mice. All mouse strains were bred and housed in specific pathogen-free conditions in accordance with the Institutional Animal Care and Use Guidelines of the University of California, San Diego (UCSD) at a temperature between 18°C and 23°C with 40–60% humidity. Male and female mice were both used in the present study. All mice used were on a C57BL/6J background. P14, *Tgfb β 2^{fl/fl}* mice (stock no. 012603, Jackson Laboratory), R26Cre-ERT2 (stock no. 008463, Jackson Laboratory), Thy1.1 and CD45.1 congenic mice were bred in house. *Prdm1^{fl/fl}* (stock no. 008100, Jackson Laboratory) and *Gzmb-cre* (stock no. 003734, Jackson Laboratory) spleens were a gift from the laboratory of S. Kaech. To delete floxed alleles using Cre-ER², we administered 1 mg of tamoxifen (Cayman Chemical Company) emulsified in 100 μ l of sunflower seed oil (Sigma-Aldrich) via daily intraperitoneal injections on days 14–18 of infection. All animal studies were approved by the Institutional Animal Care and Use Committees of UCSD and performed in accordance with UC guidelines.

Cell culture. PLAT-E cells were cultured in Dulbecco's modified Eagle's medium + D-glucose supplemented with 10% bovine growth serum, 100 U ml⁻¹ of penicillin, 100 μ g ml⁻¹ of streptomycin, 292 μ g ml⁻¹ of L-glutamine, 10 mM Hepes and 55 μ M 2-mercaptoethanol. Enriched CD8⁺ T cells were maintained in RPMI + L-glutamine supplemented with 10% fetal bovine serum (FBS), 100 U ml⁻¹ of penicillin, 100 μ g ml⁻¹ of streptomycin, 292 μ g ml⁻¹ of L-glutamine, 10 mM Hepes and 55 μ M 2-mercaptoethanol.

Infection studies. C57BL/6J P14 CD8⁺ T cells congenic for CD45 or Thy1 were adoptively transferred at 5 \times 10⁴ cells per recipient mouse by intravenous (i.v.) injection. Donor mice were sex and age matched to recipients or female donors were transferred into male recipients. For cotransfers, *Tgfb β 2^{fl/fl}ER-Cre⁺* and the corresponding control P14 CD8⁺ T cells were mixed in a 1:1 ratio and adoptively transferred by i.v. injection into CD45 or Thy1 congenic recipients. Mice were then infected with 2 \times 10⁵ plaque-forming units (p.f.u.) of LCMV Armstrong by intraperitoneal (i.p.) injection or with 5 \times 10³ colony-forming units (c.f.u.) of LM-gp33 by i.v. injection 24 h after transfer. For cotransfers of transduced cells, P14 cells were mixed at a 1:1 ratio of ametrine⁺ cells and a total of 5 \times 10⁵ P14 cells was transferred by i.v. injection into CD45 or Thy1 congenic recipients. Then, 1 h after transfer, recipient mice were infected with either 2 \times 10⁵ p.f.u. of LCMV by i.p. injection or 5 \times 10³ c.f.u. of LM-gp33 by i.v. injection.

Preparation of single-cell suspensions. To identify CD8⁺ T cells in the vasculature of nonlymphoid tissues (SI, kidney, SG, fat and liver), 3 μ g of CD8 α (53-6.7) conjugated to APC-eFluor 780 was injected intravenously into mice 3 min before sacrifice, as has been previously described¹. Cells labeled with low to no CD8 α antibody were considered to be outside the vasculature. Single-cell suspensions of splenocytes were prepared by mechanical disaggregation followed by treatment with ACK (ammonium-chloride-potassium) lysing buffer. Blood samples were treated with ACK lysing buffer. SI IEL were prepared through the removal of Peyer's patches and the luminal contents. The SI was cut longitudinally and into 1-cm pieces, then incubated at 37°C for 30 min in Hanks' balanced salt solution with 2.1 mg ml⁻¹ of sodium bicarbonate, 2.4 mg ml⁻¹ of Hepes, 8% bovine growth serum and 0.154 mg ml⁻¹ of DTE (EMD Millipore). The kidneys, SG, fat and liver were minced into small pieces and then incubated in RPMI with 1.2 mg ml⁻¹ of Hepes, 292 μ g ml⁻¹ of L-glutamine, 1 mM MgCl₂, 1 mM CaCl₂, 5% FBS and 100 U ml⁻¹ of collagenase (Worthington) at 37°C for 30 min. Lymphocytes from the SI, kidney, SG and liver were separated on a 44%/67% Percoll density gradient. For digestion with cold active protease, the kidney and SG were minced into small pieces and then shaken at 4°C for 30 min in phosphate-buffered saline (PBS) with 10 mg ml⁻¹ of protease from *Bacillus* sp. (Sigma-Aldrich), 0.5 mM EDTA and 125 U ml⁻¹ of DNase (Sigma-Aldrich). Digestion was quenched with an equal volume of PBS containing 20% bovine growth serum. Lymphocytes were separated using a 44%/67% Percoll density gradient.

Generation of retroviral supernatant and CD8⁺ T cell transduction. PLAT-E cells were plated in a 10-cm tissue culture dish 1 d before transfection. The next day, each plate was transfected with 5 μ g of pCL-Eco and 10 μ g of the plasmid of interest using TransIT-LT1 (Mirus). Retroviral supernatant was collected 48 and 72 h after transfection. CD8⁺ T cells were isolated from the spleen and lymph nodes and negatively enriched, as previously described³³, then 2 \times 10⁵ P14 cells were plated in a 6-well dish coated with goat anti-hamster immunoglobulin (Ig) G (H (heavy) + L (light); Thermo Fisher Scientific), anti-CD3 (catalog no. 145-2C11, eBioscience) and anti-CD28 (catalog no. 37.51, eBioscience). Then, 18 h after plating, T cell culture medium was removed and replaced with retroviral supernatant supplemented with 50 μ M 2-mercaptoethanol and 8 μ g ml⁻¹ of polybrene (Millipore). CD8⁺ T cells were spininfected for 60 min at 800g and 37°C; 2 h after spinfection, the retroviral supernatant was removed and replaced with T cell culture medium. Then 24 h after transduction, all ametrine⁺ cells as assessed by flow cytometry were considered to be transduced.

Flow cytometry and cell sorting. Cells were incubated with the indicated antibodies for 20 min at 4°C in PBS supplemented with 2% bovine growth serum and 0.01% sodium azide. Intracellular staining was completed using the

FoxP3 transcription factor staining kit (eBioscience). For assays with CD8⁺ T cell stimulation, P14 cells from each tissue were incubated for 3 h in T cell culture medium at 37°C with 10 nM GP33–41 peptide and Protein Transport Inhibitor (eBioscience) (see Supplementary Table 7 for a list of antibodies used in the present study). Stained cells were analyzed using LSRFortessa or LSRFortessa X-20 cytometers (BD), FACSDiva software and Flowjo software (TreeStar). All sorting was performed on BD FACSAria Fusion instruments.

Bulk RNA-seq. For each replicate, cells from 10–15 mice were pooled and then sorted for bulk RNA-seq. Then, 32 d after initial infection with LCMV, 5 \times 10³ P14 cells were sorted from the spleen and blood and 5 \times 10³ IV- P14 cells were sorted from the IEL, kidney, SG, fat and liver into PBS + 5% bovine serum albumin (BSA). Cells, 1 \times 10³, were then resorted into 1 \times TCL lysis buffer + 1% 2-mercaptoethanol. Library preparation for ultra-low-input RNA-seq was performed as described online (https://www.immgen.org/img/Protocols/ImmGenULI_RNAseq_methods.pdf).

Trimmomatic was used to remove adapters and trim low-quality reads (NexteraPE-PE.fa:2:30:10:1:TRUE LEADING:3 TRAILING:3 SLIDINGWINDOW:4:15 MINLEN:25)³⁴. Trimmed reads were then aligned to the genome M25 annotation of the mm10 genome using STAR with the default conditions⁵⁵. Aligned reads were then quantified with featureCounts⁵⁶ (-t exon -g gene_id -p -B) and DEGs were identified using DESeq2 (ref. ⁵⁷). The list of all DEGs was generated by combining the contrasts of each tissue compared with the spleen and including all genes where the log₂(fold-change) > 1 and P_{adj} < 0.05. PCA analysis in Fig. 1 was generated with the plotPCA function in DESeq2 (ref. ⁵⁷). Clustering in Fig. 1c was performed using pheatmap with a k -mean = 8 and all heatmaps were generated using the pheatmap package. Gene set variation analysis (GSVA) was performed using the GSVA package in R⁵⁸. Raw expression counts were used as input and kcdf was set to Poisson. The TGF- β gene list was obtained from Nath et al.³⁴.

10 \times Genomics library preparation and sequencing. Cells, 1 \times 10⁴, were sorted into T cell culture medium as described above. Samples were spun down at 500 relative centrifugal force (r.c.f.) for 5 min and then resuspended in PBS + 0.04% (w:v) BSA. Samples were then loaded into Chromium Chip B (10 \times Genomics) and partitioned into Gel Bead In-Emulsions (GEMs) in a chromium controller (10 \times Genomics). ScRNA libraries were generated according to the Chromium Single Cell 3' Reagent Kits v.3 User Guide and sequenced on a HiSeq 4000.

Reads were aligned to the mm10 genome using cellranger count⁵⁹. The resulting counts matrix was then processed using Seurat⁶⁰ and cells with <500 or >2,500 detected genes or a mitochondrial read percentage >10 were discarded. For analysis of P14 cells across all tissues, all samples were combined into a counts matrix using the merge function in Seurat. Data were log(normalized) and scaled using NormalizeData and ScaleData. The top 2,000 most variable genes were calculated using FindVariableGenes and then used in the PCA calculation with RunPCA. The top 20 PCs were used to calculate a UMAP dimensional reduction using the RunUMAP function. Louvain clustering was performed with Seurat's FindClusters based on the top 20 PCs with the resolution set to 0.35. For visualizing the intra-tissue heterogeneity, each tissue dataset was normalized separately using sctransform in Seurat. The top ten genes, as ranked by residual variance after running sctransform for each tissue, were plotted. In addition, data imputation was performed using MAGIC⁶¹ with the log(normalized expression) values and the default settings and the exact solver. Seurat's AddModuleScore with default settings function was used to calculate scores for the TGF- β gene list (Supplementary Table 8).

The human single-cell data were normalized using scuttle's logNormCounts after running quickCluster with the patient ID as a blocking factor. Cell type was annotated using SingleR⁶² with the MonacoImmuneData as a reference. Subsequently the dataset was filtered on T cells and patients with ulcerative colitis were excluded. The TGF- β and T_{RM} signature score were calculated using AUCell⁶³.

ATAC-seq. For each replicate, cells from 10–15 mice were pooled and then 2 \times 10⁴ cells were sorted into PBS + 5% BSA and spun down at 500g for 20 min at 4°C. The cell pellet was resuspended in 25 μ l of lysis buffer and then spun down at 600g for 30 min at 4°C. The nuclei pellet was resuspended in 25 μ l of transposition reaction mixture containing Tn5 transposase from Nextera DNA Sample Prep Kit (Illumina) and incubated at 37°C for 30 min. The transposase-associated DNA was then purified using the Zymo DNA clean-up kit. To amplify the library, the DNA was first amplified for five cycles using indexing primers from the Nextera kit and NEBNext High-Fidelity 2 \times PCR master mix. To reduce the PCR amplification bias, after the first 5 cycles, 5 μ l of amplified DNA was used to perform qPCR to determine the number of cycles for the second round of PCR. The total amplified DNA was then size selected to fragments <800 bp using gel purification. The size of the pooled library was examined by tapestation. The final library was then sequenced on a HiSeq 4000 to get at least 10 million reads. Sequencing results were initially analyzed and processed using the ENCODE ATAC-seq pipeline, including read trimming, quality filtering, alignment and peak calling^{64,65}. We performed each ATAC-seq experiment at least twice and used the irreproducibility discovery rate framework to identify the reproducible peaks. DARs were identified

using diffbind⁶⁶, filtering out regions with <20 reads in any sample or less than a fourfold difference in the number of reads between the spleen and any other tissue. Heatmaps were generated using pheatmap. PageRank analysis was performed as previously described^{35–37}. As outlined above, the normalized counts table generated for the RNA-seq data, the alignment files generated by the ATAC-seq pipeline and the optimal peaks list were used as the inputs for this analysis.

LCMV titers by qPCR. Tissues were homogenized and RNA was extracted. Complementary DNA was synthesized using the superscript IV transcriptase. The following primers were used for *Hprt* (forward: TGAAGAGCTACTGTAA TGATCAGTCAAC; reverse: AGCAAGCTTGCAACCTTAACCA) and LCMV gp (glycoprotein) (forward: CATTCACCTGGACTTTGTCTCAGACTC; reverse: CATTCACCTGGACTTTGTCTCAGACTC).

Statistical methods. Statistical tests were performed using Prism (7.0/9.0; Graphpad) and R (v.4.1). Two-tailed, paired or unpaired Student's *t*-test, or one- or two-way analysis of variance (ANOVA) was used for comparisons between groups. *P* values <0.05 were considered significant.

Reporting summary. Further information on research design is available in the Nature Research Reporting Summary linked to this article.

Data availability

All bulk RNA-seq, ATAC-seq and scRNA-seq datasets have been uploaded to the Gene Expression Omnibus repository (accession no. GSE182276). The following published datasets were used in addition: accession nos. GSE125527 (ref. ⁴³), GSE70813 (ref. ¹⁰), GSE131847 (ref. ⁷), PRJNA414132 (ref. ²⁰), GSE117568 (ref. ⁴²), GSE63340 (ref. ¹⁷) and GSE128197 (ref. ⁴¹). The mouse reference genome mm10 has been used for RNA-seq, ATAC-seq and scRNA-seq analysis.

References

53. Chen, R. et al. In vivo RNA interference screens identify regulators of antiviral CD4⁺ and CD8⁺ T cell differentiation. *Immunity* **41**, 325–338 (2014).
54. Bolger, A. M., Lohse, M. & Usadel, B. Trimmomatic: a flexible trimmer for Illumina sequence data. *Bioinformatics* **30**, 2114–2120 (2014).
55. Dobin, A. et al. STAR: ultrafast universal RNA-seq aligner. *Bioinformatics* **29**, 15–21 (2013).
56. Liao, Y., Smyth, G. K. & Shi, W. featureCounts: an efficient general purpose program for assigning sequence reads to genomic features. *Bioinformatics* **30**, 923–930 (2014).
57. Love, M. I., Huber, W. & Anders, S. Moderated estimation of fold change and dispersion for RNA-seq data with DESeq2. *Genome Biol.* **15**, 550 (2014).
58. Hanzelmann, S., Castelo, R. & Guinney, J. GSEA: gene set variation analysis for microarray and RNA-seq data. *BMC Bioinf.* **14**, 7 (2013).
59. Zheng, G. X. et al. Massively parallel digital transcriptional profiling of single cells. *Nat. Commun.* **8**, 14049 (2017).
60. Stuart, T. et al. Comprehensive integration of single-cell data. *Cell* **177**, 1888–1902.e1821 (2019).

61. van Dijk, D. et al. Recovering gene interactions from single-cell data using data diffusion. *Cell* **174**, 716–729.e727 (2018).
62. Aran, D. et al. Reference-based analysis of lung single-cell sequencing reveals a transitional profibrotic macrophage. *Nat. Immunol.* **20**, 163–172 (2019).
63. Aibar, S. et al. SCENIC: single-cell regulatory network inference and clustering. *Nat. Methods* **14**, 1083–1086 (2017).
64. Consortium, E. P. An integrated encyclopedia of DNA elements in the human genome. *Nature* **489**, 57–74 (2012).
65. Davis, C. A. et al. The encyclopedia of DNA elements (ENCODE): data portal update. *Nucleic Acids Res.* **46**, D794–D801 (2018).
66. Ross-Innes, C. S. et al. Differential oestrogen receptor binding is associated with clinical outcome in breast cancer. *Nature* **481**, 389–393 (2012).

Acknowledgements

This work was funded by the National Institutes of Health (grant no. AI067545 to A.W.G. and no. AI132122 to A.W.G. and J.T.Chang) and the American Cancer Society Postdoctoral Fellowship (grant no. PF-20-048-01-LIB to J.T.Crowl). ATAC-seq and scRNA-seq using the 10× Genomics platform was conducted at the IGM Genomics Center, UCSD and supported by grant nos. P30KC063491 and P30CA023100. A.W.G. is a UCSD Tata Chancellor's Professor. M.H. was supported by the German Research Foundation fellowship (no. HE 8656/1-1). We thank H. Nguyen for assistance with measuring LCMV titers, the Goldrath laboratory members for technical advice, helpful discussion and critical reading of the manuscript and the Immunological Genome Project for reagents and sample/data processing.

Author contributions

J.T. Crowl, M.H., J.T. Chang and A.W.G. conceived the project and performed the methodology. J.T. Crowl, M.H., A.F., C.T., K.D.O., J.J.M. and Z.E. did the investigations. J.T. Crowl, M.H., A.F. and J.J.M. carried out the formal analysis. J.T. Crowl, M.H. and A.W.G. wrote the original draft of the paper. J.T. Crowl, M.H., J.T. Chang, K.D.O. and A.W.G. wrote the paper. J.T. Chang. and A.W.G. supervised the project. A.W.G. and J.T. Chang acquired the funds.

Competing interests

A.W.G. is a member of the ArsenalBio scientific advisory board. J.T. Crowl is a current employee of Outpace Bio. The remaining authors declare no competing interests.

Additional information

Extended data Extended data are available for this paper at <https://doi.org/10.1038/s41590-022-01229-8>.

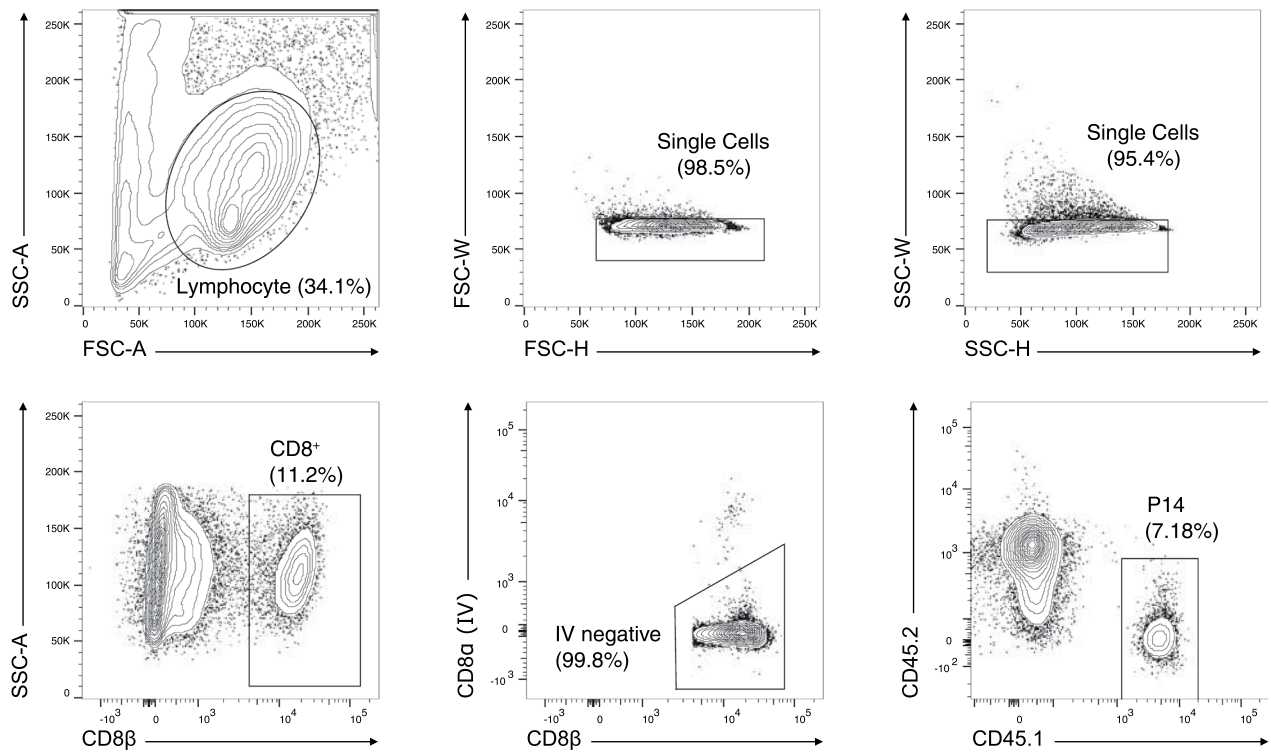
Supplementary information The online version contains supplementary material available at <https://doi.org/10.1038/s41590-022-01229-8>.

Correspondence and requests for materials should be addressed to Ananda W. Goldrath.

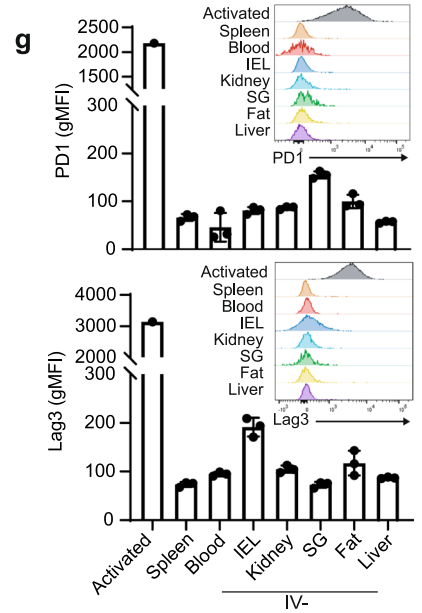
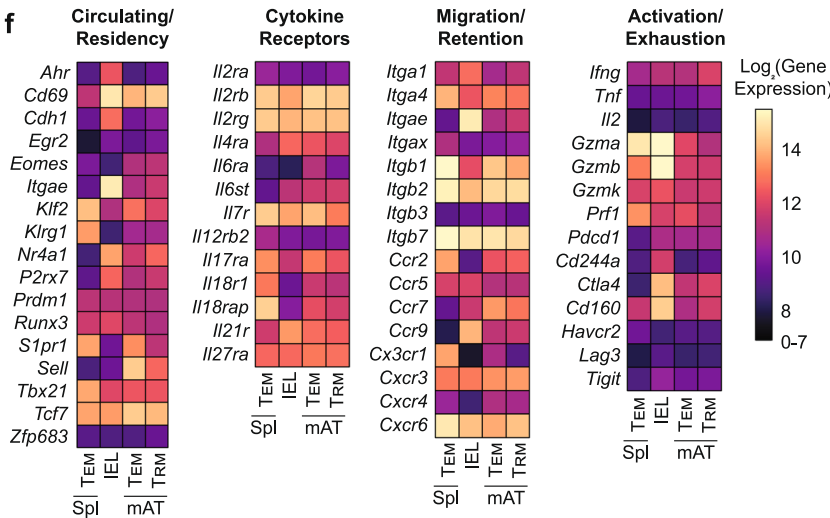
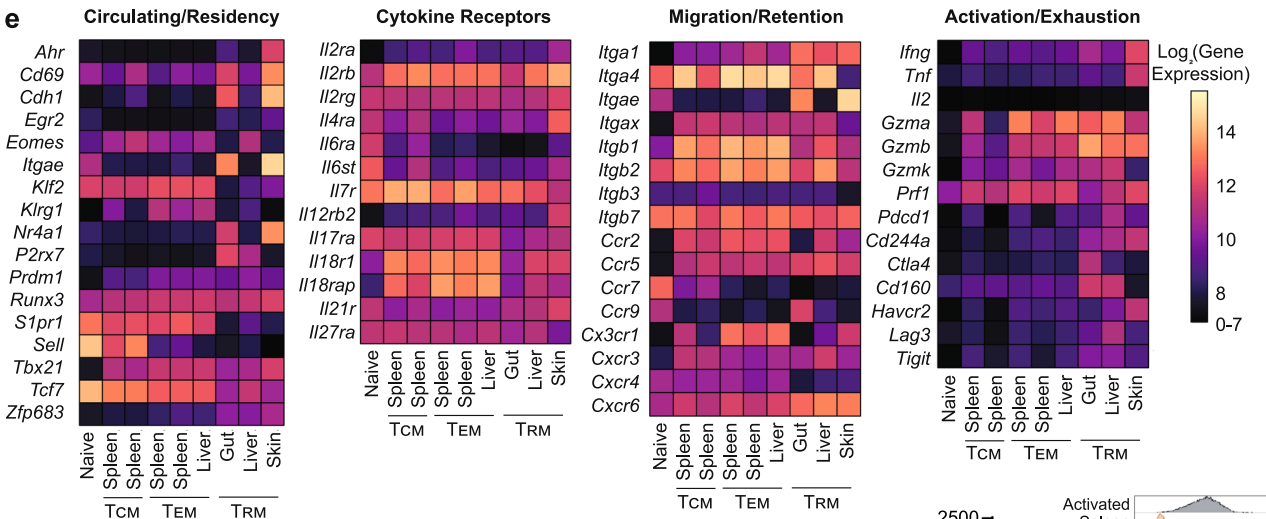
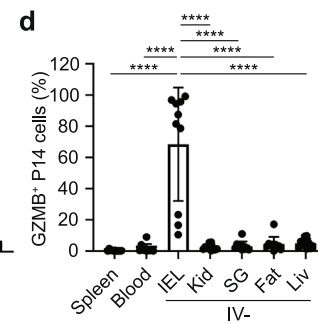
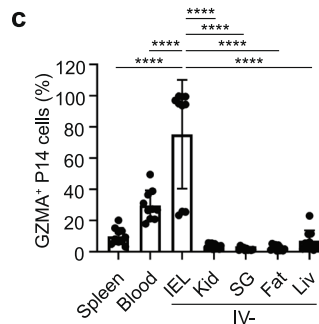
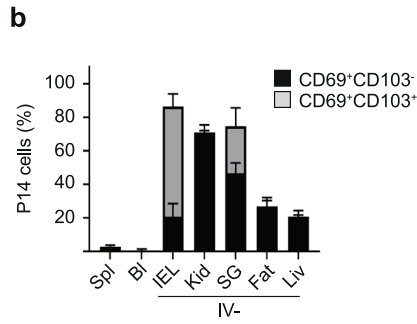
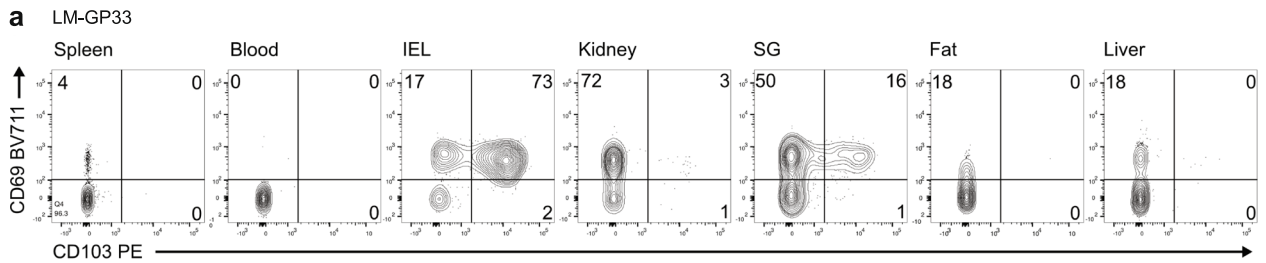
Peer review information *Nature Immunology* thanks the anonymous reviewers for their contribution to the peer review of this work. Primary Handling Editor: Ioana Visan in collaboration with the *Nature Immunology* team.

Reprints and permissions information is available at www.nature.com/reprints.

a

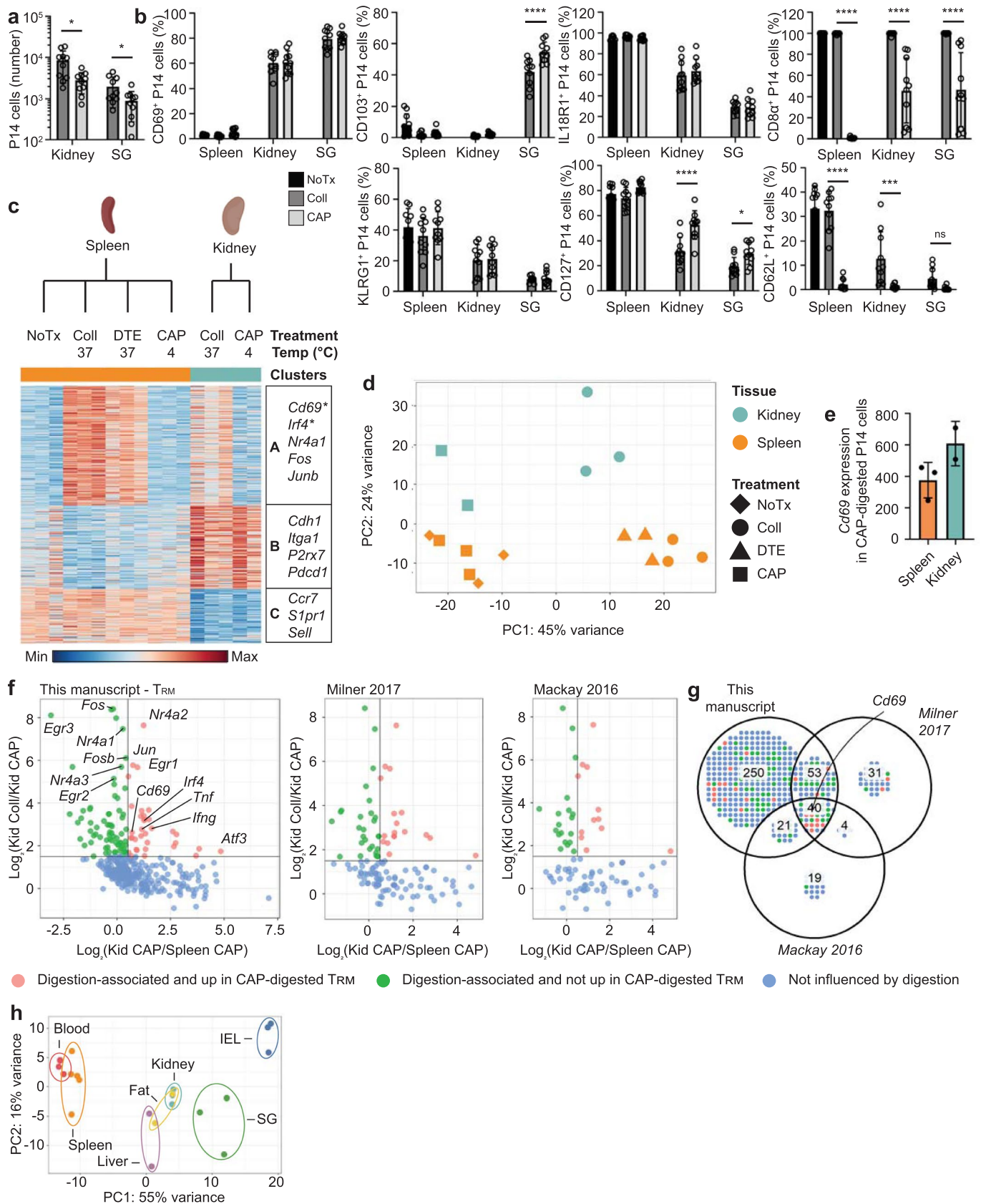


Extended Data Fig. 1 | Gating strategy. a. Gating strategy used to identify indicated IV⁻ T_{RM} populations.



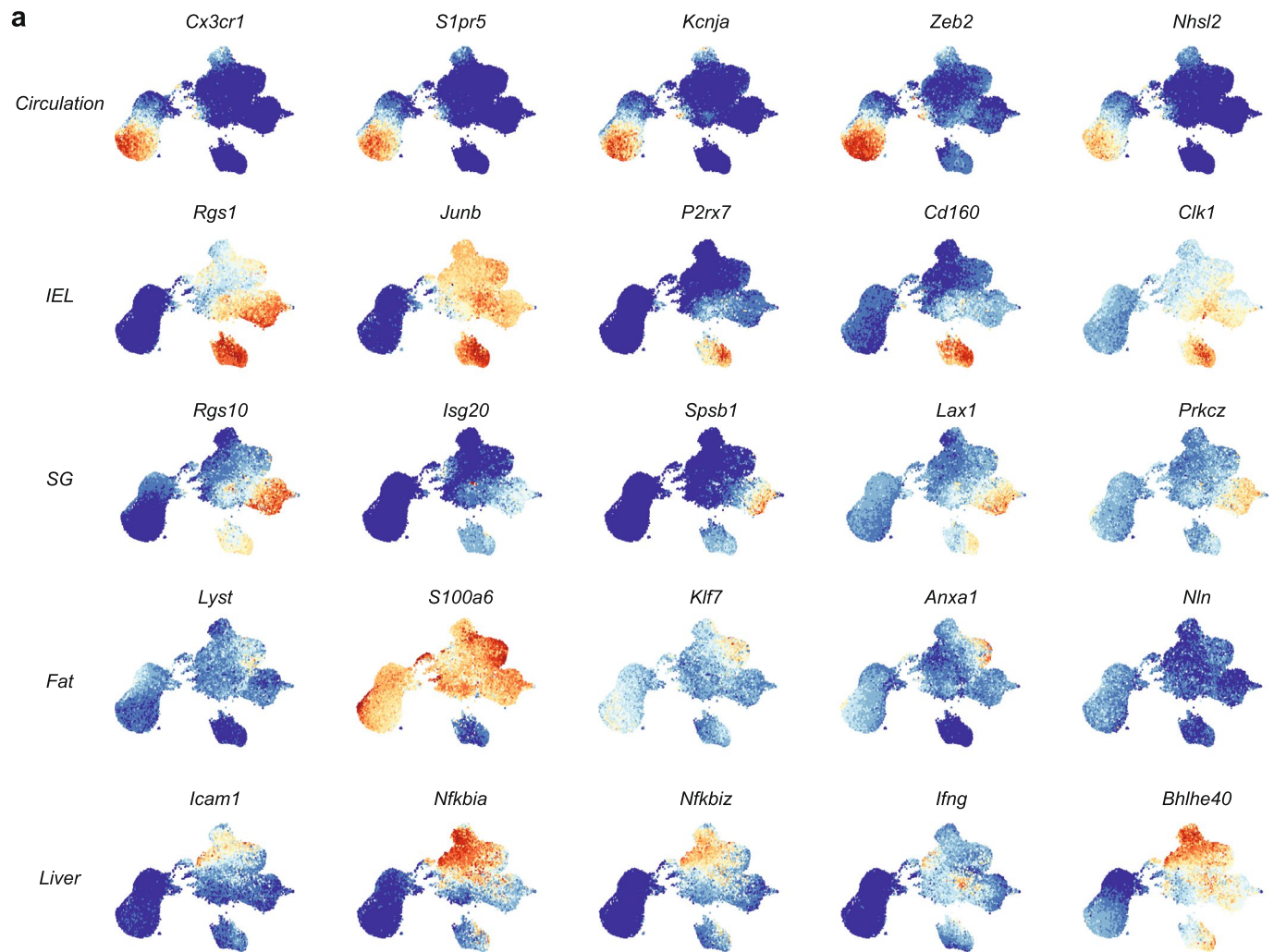
Extended Data Fig. 2 | See next page for caption.

Extended Data Fig. 2 | Phenotypic characterization of T_{RM} after LM-gp33 infection and expression of select genes in T_{RM} from other published datasets. **a-b**, CD69 and CD103 expression by CD8⁺ T_{RM} isolated from tissues 30-40 days after infection with LM-GP33. Representative flow cytometry plots (**a**) and quantification (**b**). **c-d**, Percent of GZMA⁺ (**c**) and GZMB⁺ (**d**) P14 cells isolated from the indicated tissues 30-40 days after infection with LM-GP33 as assessed by flow cytometry. Datasets are from (**e**) Mackay *et al*, *Science* 2016. (**f**) Han *et al*, *Immunity* 2017. (**g**) *ex vivo* PD1 and Lag3 expression in P14 cells isolated from the indicated tissues. Quantification of flow cytometry data in **b**, **c** and **d** displays the mean \pm SD for 10 mice from 3 experimental replicates. Data in **g** shows a representative experiment with 3 mice from a total of 3 experiments with 10 mice. Significance was calculated using a one-way ANOVA and corrected for multiple comparisons using Tukey's test. **** $p < 0.0001$.

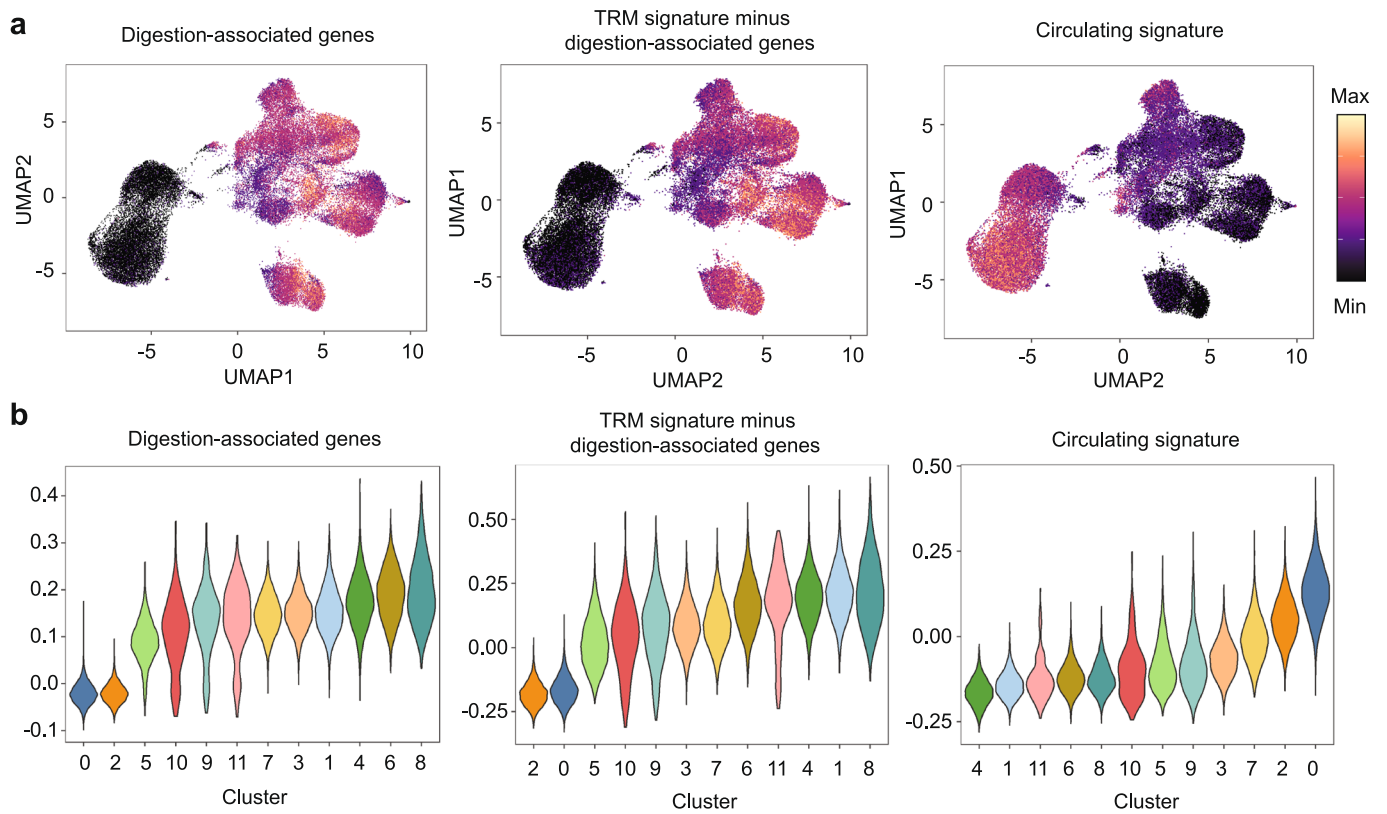


Extended Data Fig. 3 | See next page for caption.

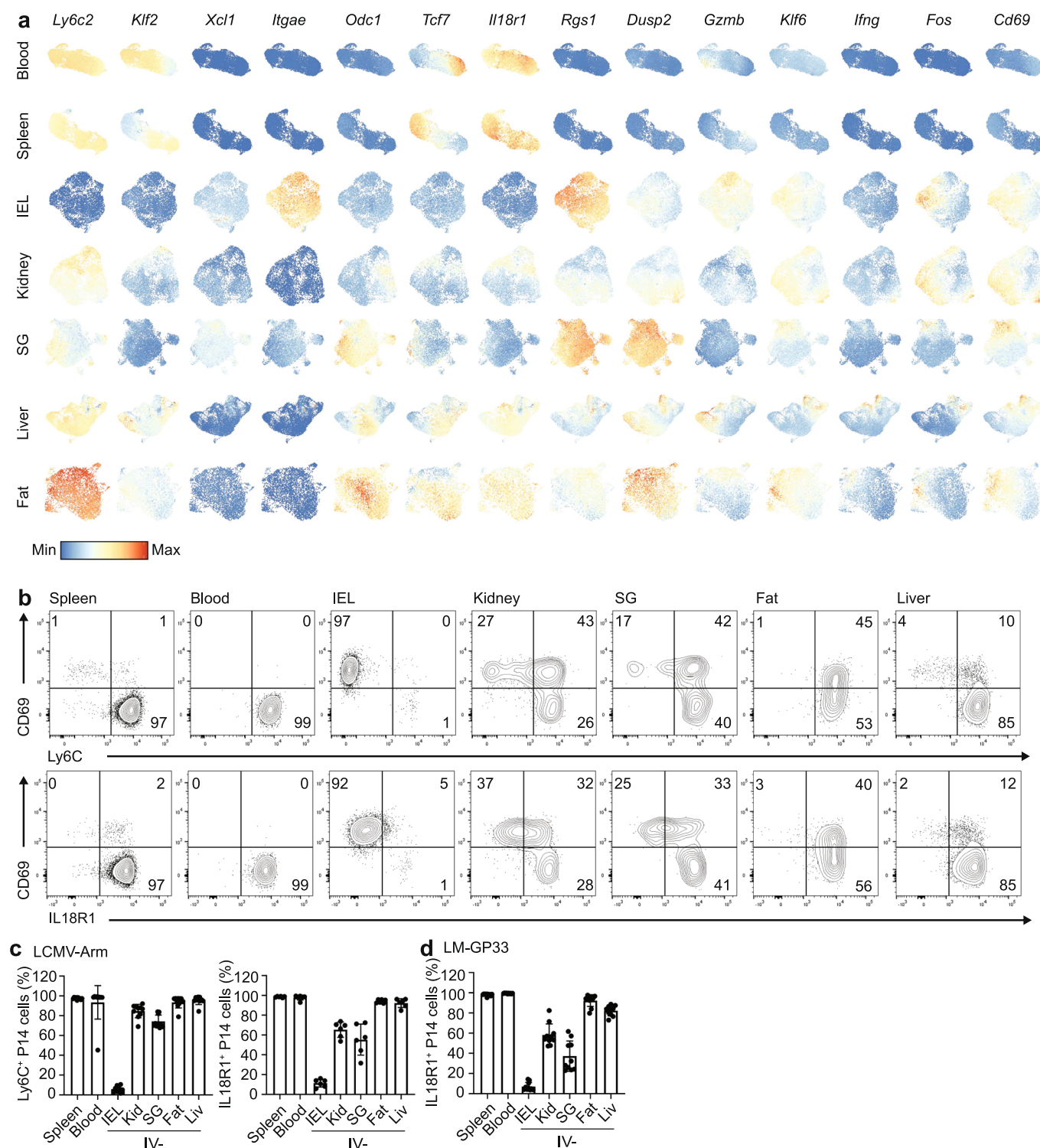
Extended Data Fig. 3 | Collagenase digestion induces upregulation of a subset of genes also associated with tissue residency. a-d, P14 cells were adoptively transferred into CD45 congenic hosts one day prior to infection with LCMV. 30–40 days after initial infection, P14 cells were isolated from tissues using no additional treatment (NoTx), collagenase (Coll), or a cold active protease (CAP). **a**, Quantification of the number of P14 cells recovered from each tissue using the indicated digestion methods. **b**, Percent of P14 cells expressing CD69 (top left), CD103 (top center left), IL-18R1 (top center right), CD8a (top right), KLRG1 (bottom left), CD127 (bottom center), or CD62L (bottom right) assessed by flow cytometry. **c-e**, RNA-sequencing of P14 cells isolated from the spleen or kidney using NoTx, Coll, dithioerythritol (DTE), or CAP. **c**, Differentially expressed genes (348) were clustered with k-means = 3. Select genes in each cluster displayed on the right. Genes that were upregulated in CAP-treated tissues compared to CAP-treated spleens indicated with an asterisk. **d**, Principal Component Analysis. **e**, *Cd69* expression by P14 cells isolated from the spleen or kidney with CAP. **f,g**, Genes included in the T_{RM} signatures from this paper (left), *Milner et al, Nature 2017* (center) and *Mackay et al, Science 2016* (right) were selected. **f**, Corresponding expression values for collagenase-digested kidney, CAP-digested kidney, and CAP-digested spleen samples were plotted. Each gene in the corresponding T_{RM} signature is represented by a single point and colored by influence of digestion on expression. **g**, Venn diagram of the preceding data. **h**, Principal component analysis of RNA-sequencing data from Fig. 1 with all digestion-associated genes removed. Genes were considered digestion-associated if they were expressed above a minimum threshold and at >1.5 fold in collagenase-digested kidney compared to CAP-digested kidney samples. Graphs in **a** and **b** display the mean \pm SD for 10 mice from 3 experimental replicates. RNA-seq data displayed in **c-f** contains 2–3 experimental replicates for each sample, and tissues from multiple mice were pooled. Graph in **e** displays the mean \pm SD. Significance calculated using a two-way ANOVA and correcting for multiple comparisons using Dunnett's test. * $p < 0.05$, *** $p < 0.001$, **** $p < 0.0001$.



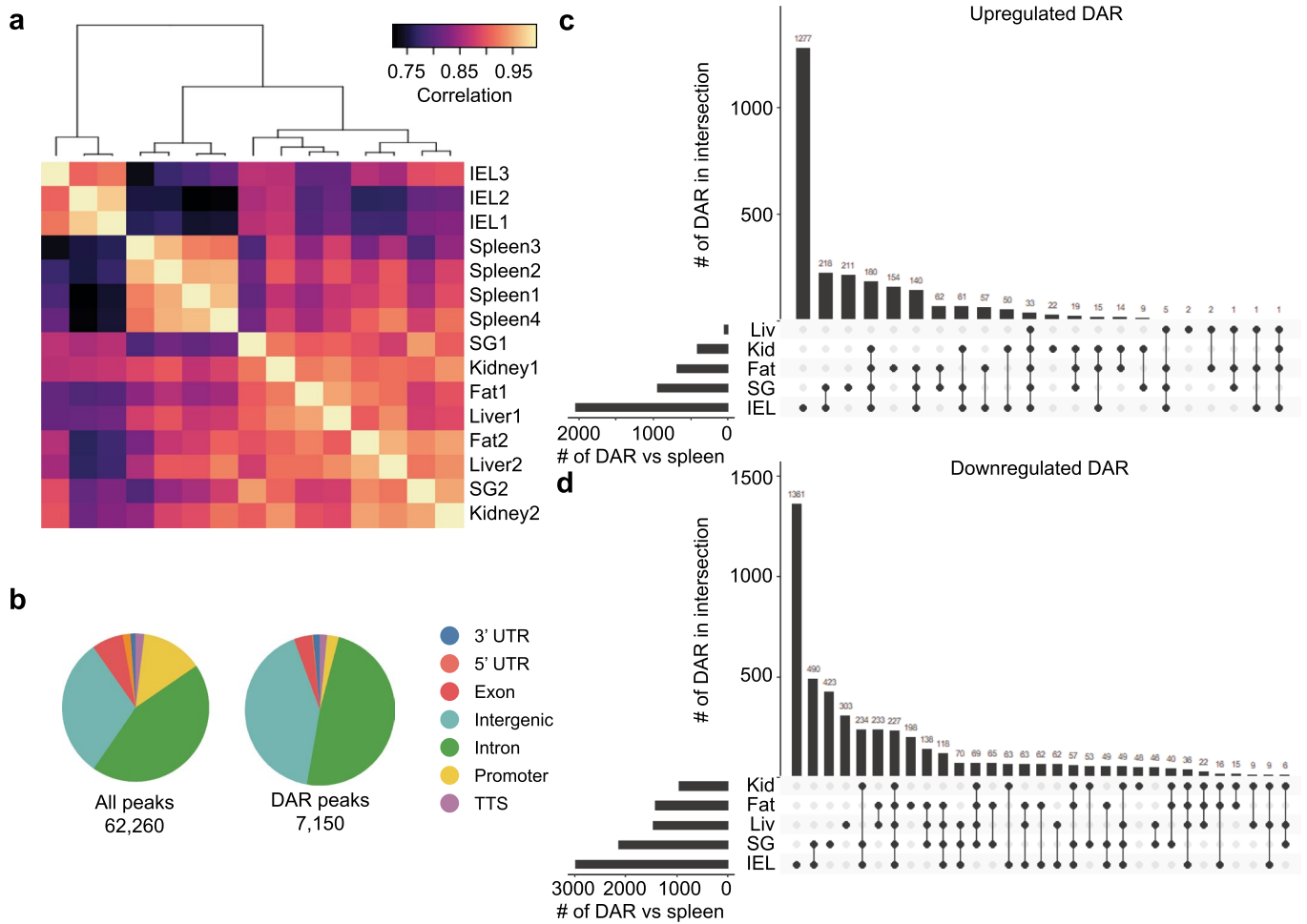
Extended Data Fig. 4 | Top enriched genes identified in bulk RNA-seq of T_{RM} are also found in scRNA-seq. a. The top 5 genes enriched in bulk RNA-seq samples for T_{RM} isolated from the blood, IEL, SG, fat, and liver are shown on a UMAP dimensional reduction plot.



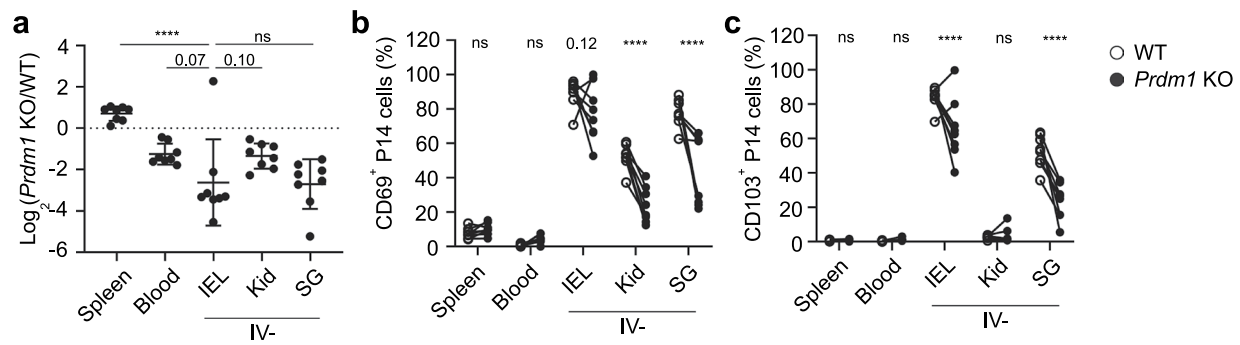
Extended Data Fig. 5 | Removal of digestion-associated gene signature from the T_{RM} gene signature does not alter the enrichment of tissue signature. **a,b**, scRNA-sequencing data described in Fig. 2. Each cell was scored based on the enrichment of genes included in the indicated signatures. Cells were colored by score on a UMAP dimensional reduction (**a**) and separated by cluster and ordered based on score (**b**).



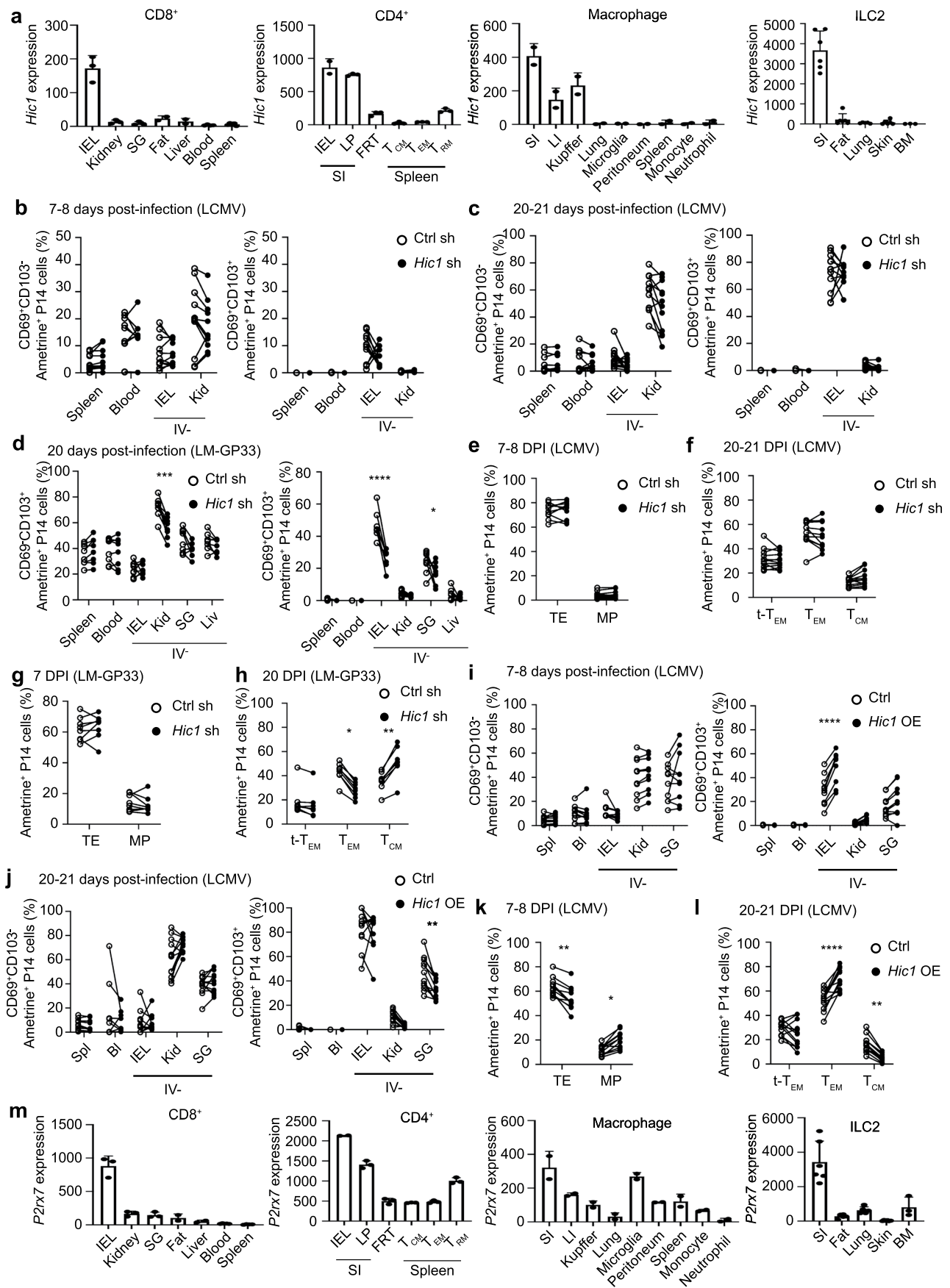
Extended Data Fig. 6 | T_{RM} differentiation programs are a source of intra-tissue heterogeneity. **a**, UMAP dimensional reduction of scRNA-sequencing of T_{RM} separated by tissue. Cells were colored by the expression of the indicated genes. Scales are consistent across tissues to allow for comparison within and among tissues. **b-c**, Expression of CD69, Ly6C, IL18R1 on P14 cells harvested 30-40 days after initial infection with LCMV. Representative flow cytometry plots (**b**) and quantification (**c**). **d**, Quantification of IL18R1 expression on P14 cells harvested from the indicated tissues 30-40 days after initial infection with LM-GP33. Quantification of flow cytometry data in **c** and **d** displays the mean \pm SD for 6 (c) 10 (d) mice from 2 experimental replicates.



Extended Data Fig. 7 | T_{RM} in distinct tissue microenvironments possess unique epigenetic programs. a-d, ATAC-seq of P14 CD8⁺ T cells in the spleen and IV⁻ P14 CD8⁺ T cells isolated from the IEL, kidney, SG, fat, and liver. **a**, Pearson correlation for all peaks across all samples. **b**, Annotation of the genomic region type for all identified accessible regions (left) and DAR (right). **c,d**, Shared and unique upregulated DAR (**c**) and downregulated DAR (**d**) in each tissue compared to the spleen for all DAR with a p-value <0.05 and a fold change >4 using a Wald statistics.

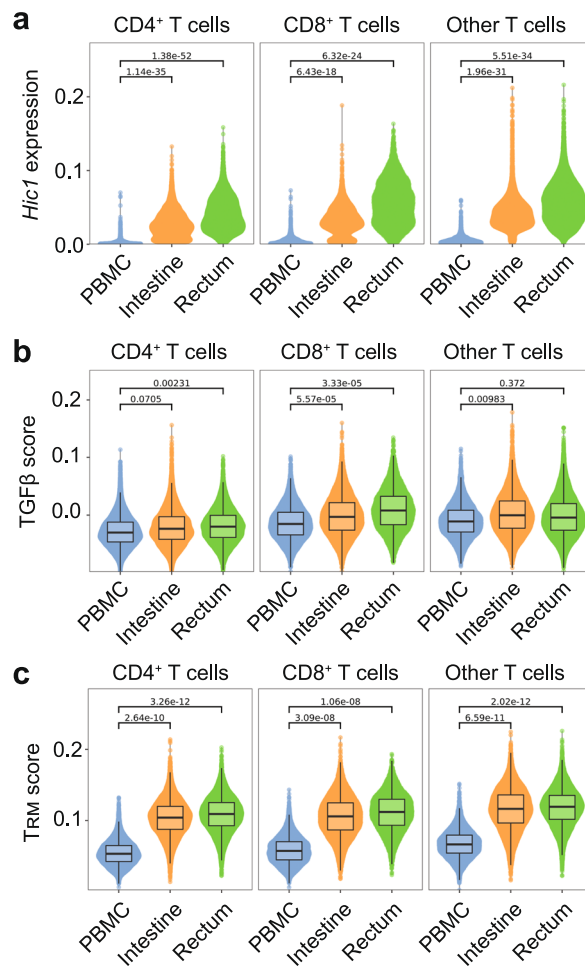


Extended Data Fig. 8 | Blimp1 deletion impairs T_{RM} formation in the IEL and SG more than the kidney. **a-c**, *Gzmb-Cre^{-/-}Prdm1^{fl/fl}* (WT) and *Gzmb-Cre^{+/-}Prdm1^{fl/fl}* (KO) were transferred at a 1:1 ratio into congenically distinct recipients one day prior to infection with LCMV. Tissues were harvested 60 days after initial infection. **a**, Ratio of KO to WT P14 cells in the indicated tissues. **b-c**, % of CD69⁺ (**b**) and CD103⁺ (**c**) P14 cells for WT and KO populations. Graphs display mean \pm SD for a combined 2 experimental replicates, each with $m = 4$ mice. Significance in (**a**) calculated with a one-way ANOVA using Tukey's multiple comparison test. Significance in (**b-c**) calculated with a two-way ANOVA using with Sidak's multiple comparison test. **** $p < 0.0001$.



Extended Data Fig. 9 | See next page for caption.

Extended Data Fig. 9 | Hic1 is critical for the differentiation of small intestine T_{RM}. **a**, *Hic1* expression by resident immune cell populations isolated from the indicated tissues. **b-g**, 1:1 mixed transfer of P14 cells transduced with a control shRNA or a *Hic1*-targeting shRNA. **b-c**, Percentage of P14 cells that are CD69⁺CD103⁻ (left) or CD69⁺CD103⁺ (right) on day 7-8 (**b**) or day 20-21 post-infection with LCMV (**c**). **d**, Percentage of P14 cells that are CD69⁺CD103⁻ (left) or CD69⁺CD103⁺ (right) on day 20 post-infection with LM-GP33. **e**, Percentage of P14 cells that were terminal effectors (TE, KLRG1⁺CD127⁻) or memory precursors (MP, KLRG1⁻CD127⁺) on day 7-8 post-infection with LCMV. **f**, Percentage of P14 cells that are terminal effector memory (tTEM, CD127⁻CD62L⁻), effector memory (TEM, CD127⁺CD62L⁻), or central memory (TCM, CD127⁺CD62L⁺) on day 20-21 post-infection with LCMV. **g-h**, Percentage of P14 cells that were TE or MP on day 7 (**g**) or day 20 (**h**) after infection with LM-GP33. **i-l**, 1:1 mixed transfer of P14 cells transduced with a control vector or a *Hic1*-overexpression vector. **i-j**, Percentage of P14 cells that are CD69⁺CD103⁻ (left) or CD69⁺CD103⁺ (right) on day 7-8 (**i**) or day 20-21 (**j**) post-infection with LCMV. **k**, Percentage of P14 cells that were TE or MP on day 7-8 post-infection with LCMV. **l**, Percentage of P14 cells that were tTEM, TEM, or TCM on day 20-21 post-infection with LCMV. **m**, *P2xr7* expression by resident immune cell populations isolated from the indicated tissues. Graphs in **a** and **m** display mean \pm SD for the expression values from RNA-Seq samples (22 samples for CD8⁺, 17 samples for CD4⁺, 18 samples for Macrophages, 26 samples for ILC2). Graphs in **b**, **c**, **e**, **f**, **il** display mean \pm SD for 11 mice from 3 experimental replicates. Graphs in **d**, **g**, and **h** display mean \pm SD for 8 mice from 2 individual experiments. Significance calculated with a two-way ANOVA using with Sidak's multiple comparison test. **p* < 0.05, ***p* < 0.01, ****p* < 0.001, *****p* < 0.0001.



Extended Data Fig. 10 | Human T_{RM} recapitulate phenotypes observed in murine T_{RM} . a-c, Single-cell RNA-sequencing of healthy human tissue in Boland *et al*, *Science Immunology* 2020. **a**, *Hic1* expression after MAGIC imputation. **b,c**, Individual cells are scored based on enrichment for genes included in the TGFβ signature (**b**) and T_{RM} signature (**c**). Single cell data was pooled from 13 different healthy donors for PBMC and rectum biopsies and 10 healthy donors for intestinal samples. Boxplot shows median. The lower and upper hinges correspond to the first and third quartiles. The upper whisker extends from the hinge to the largest value no further than 1.5 * IQR from the hinge. Statistics were calculated by aggregating the scRNA data to pseudo-bulk samples for each patient and cell type. A T statistics test as implemented in the R package limma was then used to calculate the P values.

Reporting Summary

Nature Portfolio wishes to improve the reproducibility of the work that we publish. This form provides structure for consistency and transparency in reporting. For further information on Nature Portfolio policies, see our [Editorial Policies](#) and the [Editorial Policy Checklist](#).

Statistics

For all statistical analyses, confirm that the following items are present in the figure legend, table legend, main text, or Methods section.

n/a Confirmed

- The exact sample size (n) for each experimental group/condition, given as a discrete number and unit of measurement
- A statement on whether measurements were taken from distinct samples or whether the same sample was measured repeatedly
- The statistical test(s) used AND whether they are one- or two-sided
Only common tests should be described solely by name; describe more complex techniques in the Methods section.
- A description of all covariates tested
- A description of any assumptions or corrections, such as tests of normality and adjustment for multiple comparisons
- A full description of the statistical parameters including central tendency (e.g. means) or other basic estimates (e.g. regression coefficient) AND variation (e.g. standard deviation) or associated estimates of uncertainty (e.g. confidence intervals)
- For null hypothesis testing, the test statistic (e.g. F , t , r) with confidence intervals, effect sizes, degrees of freedom and P value noted
Give P values as exact values whenever suitable.
- For Bayesian analysis, information on the choice of priors and Markov chain Monte Carlo settings
- For hierarchical and complex designs, identification of the appropriate level for tests and full reporting of outcomes
- Estimates of effect sizes (e.g. Cohen's d , Pearson's r), indicating how they were calculated

Our web collection on [statistics for biologists](#) contains articles on many of the points above.

Software and code

Policy information about [availability of computer code](#)

Data collection

Data analysis

For manuscripts utilizing custom algorithms or software that are central to the research but not yet described in published literature, software must be made available to editors and reviewers. We strongly encourage code deposition in a community repository (e.g. GitHub). See the Nature Portfolio [guidelines for submitting code & software](#) for further information.

Data

Policy information about [availability of data](#)

All manuscripts must include a [data availability statement](#). This statement should provide the following information, where applicable:

- Accession codes, unique identifiers, or web links for publicly available datasets
- A description of any restrictions on data availability
- For clinical datasets or third party data, please ensure that the statement adheres to our [policy](#)

All bulk RNA-seq, ATAC-seq, and single-cell RNA-seq data sets have been uploaded to the GEO repository and can be accessed here:
<https://www.ncbi.nlm.nih.gov/geo/query/acc.cgi?acc=GSE182276>

The following published datasets were used in addition: GSE12552751, GSE70813 10, GSE131847 7, PRJNA414132 20, GSE11756848, GSE6334017, GSE12819747.

The mouse reference genome mm10 has been used for RNA-Seq, ATAC-Seq and scRNA-Seq analysis

Field-specific reporting

Please select the one below that is the best fit for your research. If you are not sure, read the appropriate sections before making your selection.

- Life sciences Behavioural & social sciences Ecological, evolutionary & environmental sciences

For a reference copy of the document with all sections, see [nature.com/documents/nr-reporting-summary-flat.pdf](https://www.nature.com/documents/nr-reporting-summary-flat.pdf)

Life sciences study design

All studies must disclose on these points even when the disclosure is negative.

Sample size	Sample sizes were determined through prior studies from our lab. No statistical methods were used to pre-determine sample sizes but our sample sizes are similar to those reported in previous publications (e.g. Milner et al, Nature 2017)
Data exclusions	Data was excluded only under rare circumstances including: 1. Donor T cells were rejected by recipient mice.
Replication	All experiments were successfully repeated 2-3 times, and where possible quantification and statistics are run on combined replicate experiments.
Randomization	As nearly all experiments in this study compared tissues within individual mice or utilized mixed adoptive transfers to directly compare different populations of transduced T cells, recipient mice were not randomly assigned to groups. However, for the mixed adoptive transfers, care was taken to place controls on distinct CD45 congenic backgrounds in subsequent experiments.
Blinding	No blinding was performed during mouse experiments, as all mice in mixed transfers received identical treatment.

Reporting for specific materials, systems and methods

We require information from authors about some types of materials, experimental systems and methods used in many studies. Here, indicate whether each material, system or method listed is relevant to your study. If you are not sure if a list item applies to your research, read the appropriate section before selecting a response.

Materials & experimental systems

Methods

n/a	Involvement in the study	n/a	Involvement in the study
<input type="checkbox"/>	<input checked="" type="checkbox"/> Antibodies	<input checked="" type="checkbox"/>	<input type="checkbox"/> ChIP-seq
<input type="checkbox"/>	<input checked="" type="checkbox"/> Eukaryotic cell lines	<input type="checkbox"/>	<input checked="" type="checkbox"/> Flow cytometry
<input checked="" type="checkbox"/>	<input type="checkbox"/> Palaeontology and archaeology	<input checked="" type="checkbox"/>	<input type="checkbox"/> MRI-based neuroimaging
<input type="checkbox"/>	<input checked="" type="checkbox"/> Animals and other organisms		
<input checked="" type="checkbox"/>	<input type="checkbox"/> Human research participants		
<input checked="" type="checkbox"/>	<input type="checkbox"/> Clinical data		
<input checked="" type="checkbox"/>	<input type="checkbox"/> Dual use research of concern		

Antibodies

Antibodies used

Fluorophore Target Clone Vendor Cat# Dilution
 ef450 CD8B ef450 eBioH35-17.2 invitrogen 48-0083-82 400
 PerCP-Cy5.5 CD45.1 A20 invitrogen 45-0453-82 400
 APC KLRG1 2F1 Invitrogen 17-5893-82 400

PE CD103 2 E7 invitrogen 12-1031-82 100
 PE-Cy7 CD127 A7R34 invitrogen 25-1271-82 100
 APC-ef780 CD8a 53-6.7 invitrogen 47-0081-82 400
 BV510 CD62L MEL-14 BioLegend 104441 400
 BV785 CD45.2 104 BioLegend 109839 200
 BV711 CD69 H1.2F3 BioLegend 104537 200
 FITC CD127 A7R34 eBioscience 11-1271-85 100
 PerCPef710 Lag3 eBioC9B7W eBioscience 46-2231-82 200
 PE-Cy7 PD1 J43 invitrogen 25-9985-82 200
 BV785 CD45.1 A20 BioLegend 110743 400
 FITC IFN-Gamma XMG1.2 invitrogen 53-7311-82 600
 APC TNF-alpha MP6-XT22 Invitrogen 17-7321-82 100
 PE IL-2 JES6-5H4 eBioscience 12-7021-82 200
 FITC TCF1/TCF7 N/A Cell Signaling Technology 6444S 200
 PerCP-Cy5.5 CD103 2 E7 BioLegend 121416 100
 APC IL18Ralpha A17071D BioLegend 157905 200
 PE EOMES Dan11mag invitrogen 12-4875-80 50
 PE-Cy7 TBET 4B10 BioLegend 644823 200
 BV510 CD69 H1.2F3 BioLegend 104531 200
 FITC CD45.1 A20 invitrogen 11-0453-85 400
 PerCPef710 KLRG1 2F1 invitrogen 46-5893-82 400
 APC CD45.2 104 Biolegend 109824 400
 PE-Cy7 P2RX7 1F11 Biolegend 148708 200
 FITC CD8 alpha 53-6.7 TONBO biosciences 35-0081-U500 400
 APC-Cy7 CD45.2 104 BioLegend 109824 100
 FITC Ly-6C AL-21 BD Pharmingen 553104 100
 PE CXCR4 2B11 invitrogen 12-9991-81 100
 PE-Cy7 CCR9 eBioCW-1.2 invitrogen 25-1991-82 200
 FITC Granzyme B GB11 BioLegend 515403 200
 PE Granzyme A 3G8.5 BioLegend 149703 200
 Goat-anti-hamster polyclonal Invitrogen 31115 not used for flow cytometry
 anti-CD3 145-2C11 eBioscience 16-0031-85 not used for flow cytometry
 anti-CD28 37.51 eBioscience 16-0281-85 not used for flow cytometry

Validation

Fluorophore Target Validation
 ef450 CD8B ef450 tested in flow cytometry of mouse splenocytes by manufactur
 PerCP-Cy5.5 CD45.1 tested in flow cytometry of mouse splenocytes by manufactur
 APC KLRG1 tested in flow cytometry of mouse splenocytes by manufactur
 PE CD103 tested in flow cytometry of mouse splenocytes by manufactur
 PE-Cy7 CD127 tested in flow cytometry of mouse splenocytes by manufactur
 APC-ef780 CD8a tested in flow cytometry of mouse splenocytes by manufactur
 BV510 CD62L Flow Cytometry - Quality tested
 BV785 CD45.2 Flow Cytometry - Quality tested
 BV711 CD69 Flow Cytometry - Quality tested
 FITC CD127 tested in flow cytometry of mouse splenocytes by manufactur
 PerCPef710 Lag3 tested in flow cytometry of stimulated mouse splenocytes by manufactur
 PE-Cy7 PD1 tested in flow cytometry of stimulated mouse splenocytes by manufactur
 BV785 CD45.1 Flow Cytometry - Quality tested
 FITC IFN-Gamma tested in flow cytometry of stimulated mouse splenocytes by manufactur
 APC TNF-alpha tested in flow cytometry of stimulated mouse splenocytes by manufactur
 PE IL-2 tested in flow cytometry of 6-hour PMA and Ionomycin-activated mouse splenocytes by manufactur
 FITC TCF1/TCF7 tested in flow cytometry for human and mouse by manufactur
 PerCP-Cy5.5 CD103 Flow Cytometry - Quality tested
 APC IL18Ralpha Flow Cytometry - Quality tested
 PE EOMES tested in flow cytometry of mouse splenocytes by manufactur
 PE-Cy7 TBET ICFC - Quality tested
 BV510 CD69 Flow Cytometry - Quality tested
 FITC CD45.1 tested in flow cytometry of mouse splenocytes by manufactur
 PerCPef710 KLRG1 tested in flow cytometry of mouse splenocytes by manufactur
 APC CD45.2 Flow Cytometry - Quality tested
 PE-Cy7 P2RX7 Flow Cytometry - Quality tested
 FITC CD8 alpha tested in flow cytometry for mouse by manufactur
 APC-Cy7 CD45.2 Flow Cytometry - Quality tested
 FITC Ly-6C QC Testing for mouse by manufactur
 PE CXCR4 tested in flow cytometry of mouse thymocytes by manufactur
 PE-Cy7 CCR9 tested in flow cytometry of mouse thymocytes by manufactur
 FITC Granzyme B ICFC - Quality tested
 PE Granzyme A ICFC - Quality tested
 Goat-anti-hamster well-characterized specificity for hamster immunoglobulins by manufactur
 anti-CD3 tested in flow cytometry of mouse splenocytes by manufactur
 anti-CD28 tested in flow cytometry of mouse splenocytes by manufactur

Eukaryotic cell lines

Policy information about [cell lines](#)

Cell line source(s)	PlatE cells were quired from Cell Biolabs (RV-101)
Authentication	None of the cell lines were authenticated
Mycoplasma contamination	All cell lines tested negative for mycoplasma by PCR prior to use.
Commonly misidentified lines (See ICLAC register)	No commonly misidentified lines were used.

Animals and other organisms

Policy information about [studies involving animals](#); [ARRIVE guidelines](#) recommended for reporting animal research

Laboratory animals	All mice were bred and housed in specific pathogen-free conditions in accordance with the Institutional Animal Care and Use Guidelines of the University of California San Diego. P14, Tgfb β 2fl/fl mice (stock #012603, The Jackson Laboratory), R26Cre-ERT2 (stock 008463, The Jackson Laboratory), Thy1.1, and CD45.1 congenic mice were bred in house. Prdm1fl/fl (stock #008100, The Jackson Laboratory) and Gzmb-cre (stock #003734, The Jackson Laboratory) spleens were a gift from the laboratory of Dr. Susan Kaech. Both male and female mice between 6-16 weeks of age were used for these experiments.
Wild animals	The study did not involve wild animals.
Field-collected samples	The study did not involve samples collected from the field.
Ethics oversight	Institutional Animal Care and Use Committee of the University of California San Diego

Note that full information on the approval of the study protocol must also be provided in the manuscript.

Flow Cytometry

Plots

Confirm that:

- The axis labels state the marker and fluorochrome used (e.g. CD4-FITC).
- The axis scales are clearly visible. Include numbers along axes only for bottom left plot of group (a 'group' is an analysis of identical markers).
- All plots are contour plots with outliers or pseudocolor plots.
- A numerical value for number of cells or percentage (with statistics) is provided.

Methodology

Sample preparation	To identify CD8+ T cells in the vasculature of non-lymphoid tissues (small intestine, kidney, salivary gland, fat, and liver), 3 μ g of CD8 α (53-6.7) conjugated to APC eFluor780 was injected by i.v. into mice three minutes prior to sacrifice, as has been previously described. Cells labeled with low to no CD8 α antibody were considered to be outside of the vasculature. Single-cell suspensions of splenocytes were prepared by mechanical disaggregation followed by treatment with ACK lysis buffer. Blood samples were treated with ACK lysis buffer. Small intestine intraepithelial lymphocytes were prepared through the removal of Peyer's patches and the luminal contents. The small intestine was then cut longitudinally and into 1 cm pieces, then incubated at 37°C for 30 min in HBSS with 2.1 mg/mL sodium bicarbonate, 2.4 mg/mL HEPES, 8% bovine growth serum, and 0.154 mg/mL of dithioetheritol (EMD Millipore). The kidneys, salivary glands, fat, and liver were minced into small pieces and then incubated in RPMI with 1.2 mg/mL HEPES, 292 μ M L-glutamine, 1 mM MgCl $_2$, 1 mM CaCl $_2$, 5% fetal bovine serum, and 100 U/mL collagenase (Worthington) at 37°C for 30 min. Lymphocytes from the small intestine, kidney, salivary gland, and liver were separated on a 44%/67% Percoll density gradient. For digestion with cold active protease, the kidney and salivary gland were minced into small pieces and then shaken at 4°C for 30 min in PBS with 10 mg/mL protease from Bacillus Sp (Sigma), 0.5 mM EDTA, and 125 U/mL DNase (Sigma). Digestion was quenched with an equal volume of PBS containing 20% bovine growth serum. Lymphocytes were separated using a 44%/67% Percoll density gradient.
Instrument	For flow cytometry analysis, all events were acquired on a BD LSRFortessa X-20 or a BD LSRFortessa.
Software	Flowjo
Cell population abundance	Samples sorted for RNA-seq, ATAC-seq, and scRNA-seq were sorted twice sequentially to ensure a purity of > 95% for the indicated population.
Gating strategy	In all figures containing flow cytometry data, cells are initially gated on FSC-A x SSC-A and then gated on singlets. See Extended Data Fig 1. In Figure 1, 4 and Extended Data Figure 2, 3, 6: CD8B+ cells are gated on, then the congenic marker identifying transferred P14 cells. For cells from the IEL, Kidney, SG, Fat, and Liver, cells are determined to be IV- if they do not stain positive for a

CD8a antibody administered by i.v. 3 min prior to euthanizing the mouse.

For Figure 3 and Extended Data Figure 8: CD8B+ cells are gated on, then either of the congenic markers identifying the transferred P14 cells. Cells from the IEL, Kidney, SG, Fat, and Liver are determined to be IV- if they do not stain positive for a CD8a antibody administered IV 3 min prior to euthanizing the mouse. The cells are then gated based on the congenic marker identifying their genotype and distinguishing them from recipient cells.

For Figure 5, 6 and Extended Data Figure 8: CD8B+ cells are gated on, then either of the congenic markers identifying the transferred P14 cells. Cells are then gated on ametrine+ to identify transduced cells. Cells from the IEL, Kidney, SG, Fat, and Liver are determined to be IV- if they do not stain positive for a CD8a antibody administered IV 3 min prior to euthanizing the mouse. The cells are then gated based on the congenic marker identifying their genotype and distinguishing them from recipient cells.

For sorting experiments in Figure 1, 2, and 4 and Extended Data Figure 2, the gating strategy is identical to what is described for flow cytometry in Figure 1.

Tick this box to confirm that a figure exemplifying the gating strategy is provided in the Supplementary Information.